

v_2 vs p_T in p+Au at RHIC

by

Theodore Koblesky

B.S., University of Illinois, 2011

A thesis submitted to the
Faculty of the Graduate School of the
University of Colorado in partial fulfillment
of the requirements for the degree of
Doctor of Philosophy
Department of Physics
2017

This thesis entitled:
 v_2 vs p_T in p+Au at RHIC
written by Theodore Koblesky
has been approved for the Department of Physics

Prof. James Nagle

Prof. Standin

Ms. Standin

Date _____

The final copy of this thesis has been examined by the signatories, and we find that both the content and the form meet acceptable presentation standards of scholarly work in the above mentioned discipline.

Koblesky, Theodore (Ph.D., High Energy Nuclear Physics)

v_2 vs p_T in p+Au at RHIC

Thesis directed by Prof. James Nagle

Abstract

Dedication

To some of the of the fluffy kitties.

Acknowledgements

People

Contents

Chapter

1	Introduction	1
1.1	The Standard Model	1
1.2	Quantum Chromodynamics	1
1.3	Heavy Ion Collisions	2
2	Collectivity in QCD	4
2.1	Conceptual Understanding of Flow	4
2.2	Mathematical Introduction	4
2.3	A Review of Flow Measurements in Heavy Ion Collisions	5
2.4	Collectivity in Small QCD Systems	5
2.4.1	Monte-Carlo Initial Condition Characterization	6
3	Experimental Setup	8
3.1	RHIC	8
3.2	PHENIX	10
3.2.1	Forward Rapidity Detectors	11
3.2.1.1	Beam Beam Counter	11
3.2.1.2	Forward Vertex Detector	12
3.2.2	Midrapidity Detectors	13
3.2.2.1	Drift Chamber	13

3.2.2.2	Pad Chambers	16
3.2.2.3	Ring Imaging Cherenkov Detector	16
3.2.2.4	Electromagnetic Calorimeter	17
3.2.3	PHENIX Data Acquisition System	17
3.2.3.1	Triggering	18
3.2.3.2	Event Builder	19
3.2.4	Run 15	20
3.2.4.1	Beam Collision Geometry	22
3.2.5	centrality determination	22
4	Analysis	26
4.1	Direct Observables: The Building Blocks of the Measurement	26
4.1.1	Central Arm Tracks	27
4.1.1.1	Pad Chamber 3 Signalization	29
4.1.2	FVTX Clusters	29
4.1.3	BBC PMTs	31
4.2	Event Plane Method	31
4.2.1	Event Plane Flattening Calibration	34
4.2.2	Event Plane Resolution Calculation	36
4.3	Correcting for Beam Geometry	37
4.3.1	FVTX Inverse Phi Weighting	42
4.3.2	BBC Charge Weighting	43
4.3.3	Applying Weighting to v_2	46
4.4	Systematic Uncertainties	48
4.4.1	Non-Flow	51
5	Results & Discussion	53
5.1	v_2 Measurement	53

5.2 Comparison with Other Species	53
5.3 Comparison with Theory	56
5.3.1 SONIC	56
5.3.2 AMPT	56
5.3.3 IP-Glasma with Hydro	56

Bibliography	58
---------------------	-----------

Appendix

Tables

Table

3.1	An example Run15 p+Au 200 GeV relevant trigger configuration and parameters. A trigger's scale down number reduces its rate by $1/(1+\text{scale down})$.	19
3.2	Some relevant RHIC parameters from Run 15.	21
4.1	DC track quality summary.	28
4.2	Central Arm Track Cuts.	29
4.3	37
4.4	Systematic uncertainties given as a percent of the v_2 measurement. Note that the non-flow contribution is p_T dependent and the value here quoted corresponds to the highest measured p_T .	50
5.1	Initial eccentricity ε_2 of small systems at $\sqrt{s} = 200$ GeV for 0% – 5% centrality from Monte Carlo Glauber initial conditions smeared with a two-dimensional Gaussian of width $\sigma = 0.4$ fm, and IP-Glasma initial conditions.	56

Figures

Figure

1.1	TBA	3
2.1	TBA	4
2.2	TBA	6
2.3	a) IP-glasma. b) MC-KLN. c) MC-Glauber.	7
3.1	A helicopter's view of the accelerator chain in BNL starting at the Tandems (in gold) and ending at the RHIC ring (in blue). STAR and PHENIX can be seen at two of the interaction regions. The ring is 2.38 miles in length.	9
3.2	The top is a cross section diagram of the PHENIX detector from the incoming beam's perspective. The bottom is a cross section diagram of the PHENIX detector from the top down. The central arm detectors are not present in the bottom diagram.	12
3.3	The PHENIX coordinate system. The origin is in the middle of the PHENIX detector at the collision point. North and south are parallel to beam axis. East and west are transverse to the beam axis. Central detectors have a west and an east arm on either side of the beam. Forward detectors have a north and a south arm relative to the origin.	13
3.4	Photographs of the BBC detector. The left is of a single detector element consisting of a quartz Cherenkov and a PMT. The right is of one of the BBC arms, consisting of 64 detector elements.	14

3.5 The left is a photograph of half of the FVTX. The FVTX are the half disks on either end of the picture. The FVTX is only 20 cm in the z direction from the PHENIX coordinate system origin (the center of the picture. The right is a schematic of the FVTX at a slightly different angle.	15
3.6 A diagram of the DC titanium frame which encloses the detector.	15
3.7 A diagram of the X, U, and V wires in the DC.	16
3.8 Diagram of a granule. Granules are the building blocks of the PHENIX DAQ. Each detector subsystem has at least one granule.	19
3.9 Diagram of the event builder.	20
3.10 The distribution of BBC charges in p+Au 200 GeV events for different triggers. The black curve is the distribution of charges for the minbias trigger. The blue and red curves are the distributions of charges for the high multiplicity trigger. The red curve being scaled by a factor of 1/40 to show agreement with the black curve. The definition of the top 5% more central events are BBC south charges ≥ 48.0 . The plot shows the large enhancement of the number of 0-5% centrality events that are gained using the high multiplicity trigger compared to the number of 0-5% centrality from the minbias trigger alone.	21
3.11 A vector diagram illustrating the yellow and blue beam angle confirmation relative to the PHENIX coordinate system.	23
3.12 The distribution of BBC calculated z-vertex positions for events in p+Au 200 GeV. There are more events between -10 and 10 cm because of the BBC narrow trigger. .	23
3.13 The distribution of the length of physics runs.	24
3.14 Integrated luminosity from the p+Au dataset.	24

3.15 Real data for BBC Charge South (Au-going direction) shown as open circles and Glauber Monte Carlo + NBD. The colors correspond to the various percentiles relative to the total inelastic p+Au cross section, the most central 0-5% in solid red. The blue and red curves correspond to the Leve-1 trigger efficiency in all inelastic collisions and inelastic collisions producing a particle at midrapidity, respectively. The best fit NBD parameters are mu = 3.14, k = 0.47 , and the trigger firing on 84 +/- 3% of the total inelastic cross section [sigma = 1.76 barns].	25
4.1 For reference, I will show the PHENIX coordinate system here. The origin is in the middle of the PHENIX detector at the collision point. North and south are parallel to beam axis. East and west are transverse to the beam axis. Central detectors have a west and an east arm on either side of the beam. Forward detectors have a north and a south arm relative to the origin.	26
4.2 Momentum resolution $ p_{reco} - p_{gen} /p_{gen}$ (in percent) as a function of p_{reco} where p_{reco} is the reconstructed momentum and p_{gen} is the generated momentum of simulated single particle events [1].	27
4.3 The transverse momentum p_T distribution of central arm tracks. This is shown without any cuts. There are some junk tracks at high p_T	28
4.4 The distribution of n0 (number of PMTs fired in the RICH) is plotted on the left. The zed distribution is plotted on the right. The structure in the zed variable is from the structure of the DC detector.	28
4.5 The top 2 plots are the PC3 matching $d\phi$ fit in range $1.0 < pT < 1.1$ (GeV/c) as a example. The red line is the fit for the double Gaussian function, the blue line is the signal Gaussian function according to the fit and the pink line is the background Gaussian function. The bottom two plots are the same as the top 2 plots except the PC3 matching dz fit is shown instead.	30

4.6	The distribution of FVTX clusters in x and y for layers 1, 2, 3, and 4 for panels a), b), c), and d) respectively. The z-axis is counts.	31
4.7	A diagram showing the positions of the PMTs for the BBC south detector. Colored rings indicate PMTs at an approximate common radius. Each color indicates a different radius. There are five rings.	32
4.8	This is the Ψ_2 distribution projected over all z-vertex bins at different steps during the calibration. The top is from the FVTX south and the bottom is from the BBC south. The range of the Ψ_2 resolution is from $-\frac{\pi}{2}$ to $\frac{\pi}{2}$ because of the periodicity. The raw (in red) Ψ_2 distribution has a sinusoidal shape. The re-centered (in green) Ψ_2 distribution moves the peak and has a width. The flattened (in blue) Ψ_2 distribution spread out the counts so that there is uniformity. Each calibration step preserves the integral.	35
4.9	The intermediate resolution calculation steps. On the left are the raw difference between the two event planes angles and on the right is the cosine of two times that difference. The average of the distribution on the right is what is used in equation 4.15.	37

4.10 The first measurement of v_2 as a function of p_T with the FVTXs (top 2 panels) and the BBCs (bottom 2 panels) event plane for the p+Au @ 200 GeV dataset. The default resolution as shown in table TBA is used. The left panels show the event plane resolution corrected v_2 . The black points show the v_2 measurement measured using all CNT tracks. The blue and red points show the v_2 measurement made with only the west and east arms respectively. It is apparent that there is a significant splitting of the measurement depending on what set of tracks are being used to calculate v_2 which implies there are some systematic errors present. The left panels quantify the level of splitting by plotting the ratio of the east or west v_2 to the measurement made with all CNT tracks. The blue and red lines are constant fits to this ratio and the numbers in the legend are the constant fit parameter. For the FVTXs event plane, the east v_2 measurement is 16% higher on average from the all CNT track measurement and the west measurement is 28% lower on average. For the BBCs event plane, the east v_2 measurement is 56% higher and the west measurement is 33% lower on average.	38
4.11 A vector diagram illustrating the yellow and blue beam angle colliding at the origin of the x-z plane. The yellow beam stands for the Au-going beam (south-going) and blue beam stands for the p-going beam (north-going). Due to a necessity of running p+Au collisions @ 200 GeV in RHIC, the beams make an angle of 3.6 mRadians with respect to the z-axis in the x-z plane.	39

4.12 A corrected measurement of v_2 as a function of p_T with the FVTXs (top 2 panels) and the BBCs (bottom 2 panels) event plane for the p+Au @ 200 GeV dataset. The default resolution as shown in table TBA is used. The plotting conventions are the same as described in the caption of Fig 4.10. Even after correcting for the moving the detector elements back in the right place, it is apparent that there is still a significant splitting of the measurement although there is an improvement. For the FVTXs event plane, the east v_2 measurement is 13% higher on average from the all CNT track measurement and the west measurement is 21% lower on average and for the BBCs event plane, the east v_2 measurement is 27% higher on average and the west measurement is 16% lower on average.	40
4.13 On the left is a cartoon diagram illustrating η acceptance shift due to a beam offset in one of the FVTXs layers. The right plot shows the AMPT distribution of particles for pAu @ 200 GeV and the shifted η acceptance.	41
4.14 The left is the modification of the η acceptance as a function of ϕ for the FVTX first layer. The right is the calculated correction factor from this.	42
4.15 These 4 panels show the FVTX ϕ dependent cluster weighting when calculating the FVTX event plane for each layer separately for events with a collision vertex in z is around 0. As you can see there are some ϕ regions where weight factor is outside of the dotted line bounds. This indicates that either there was a severe deficit of clusters measure in the region or excess. Later, we will examine the effect of keeping these regions or cutting them out on the v_2 measurement.	44
4.16 The black is the FVTX weighting and the blue is the analytic weighting. They have good agreement.	45
4.17 Shown here is BBC the multiplicative weight factor F used when calculating the modified event plane for events where the collision vertex in z is around 0. The y-axis is the weight factor and the x-axis is the PMT number for the BBCs (there are 64 total in the BBCs).	45

4.20 Plotted is the BBC correction summary where the y-axis is the east/west v_2 ratio and the x-axis is the different subset of PMTs used to calculate the v_2 . The black markers are with the default corrections as shown in Fig 4.10. The red boxes are the corrections with the analytic weighting shown in Fig 4.14. Finally, the blue diamonds are the BBC inverse ϕ charge weighting as shown in section 4.3.2. The first column is the quantity calculated from all PMTs. columns 2 through 6 are using PMTs from certain rings as defined in Fig 4.7. Ring one is the hardest to correct. The first column should approximately be the average of all the other columns.	48
4.21 The top plots are FVTX event plane measurement corrected with inverse ϕ weighting and 20 % cut. FVTX layer three is excluded. This correction effectively eliminates the east west difference shown on the right.. The bottom plots are BBC event plane measurement corrected with inverse ϕ weighting and 20 % cut. This correction reduces the east west difference significantly.	49
4.22 The distribution of BBC PMT timing values. The x-axis is the difference between the southern BBC PMT t0 - the mean t0 in the south. The left plot is an example of a normal event, the right plot is an example pile up event. A normal event is strongly peaked at 0. A pile up event has a broad distribution and may not be centered at 0. Pile up events are when 2 or more collisions happen in the same crossing.	50
4.23 (a) The second order harmonic coefficients $c_2(p_T)$ for long range angular correlations in 0%–5% p+Au collisions, as well as for minimum bias p+p collisions. The latter are scaled down by the factor $(\sum Q^{\text{BBC-S}})_{p+p} / (\sum Q^{\text{BBC-S}})_{\text{pAu}}$. (b) The ratio of the two harmonics is plotted with the corresponding statistical errors.	51
4.24 TBA	52
5.1 The v_2 measurement of p+Au @ \sqrt{s} 200 GeV 0 – 5% centrality. Statistical and systematic errors are shown. The systematic errors are very large especially at high p_t and are dominated by non-flow.	54

5.2 v_2 of charged hadrons within $ \eta < 0.35$ in 0%–5% p+Au, d+Au, and HeAu central collisions, compared to hydrodynamic calculations using the SONIC model, matched to the same multiplicity as the data. Note that the data points shown include non-flow contributions, whose estimated magnitude is accounted for in the asymmetric systematic uncertainties.	54
5.3 TBA	55
5.4 TBA	57
5.5 TBA	57

Chapter 1

Introduction

1.1 The Standard Model

The SM (Standard Model of particle physics) is humanity's best understanding of how the fundamental building blocks reality behave. The SM as we know it today has evolved over many years, beginning with the unification of the electromagnetic and weak forces in the late 1960's. The current evolution of the SM includes four fundamental forces, listed in Table (TBA), and 17 fundamental particles, listed in Table (TBA). Calculations using the SM have been remarkably successful at making precise predictions which have been confirmed experimentally. It is one of the most rigorously tested theories in physics and has held up remarkably well to years of experimental testing.

1.2 Quantum Chromodynamics

In order to calculate things within the SM, we must turn to quantum field theory (QFT) to formally, mathematically describe the fundamental interactions in the SM. In order to calculate particles interacting via the strong force, the most relevant force at the high energies provided by hadron-hadron collisions at RHIC, we turn to QCD. Quantum chromodynamics introduces an additional quantum number to the SM and is governed by the SU(3) symmetry group. This new quantum number, labeled color, can take three values referred to as red (r), green (g), and blue (b), in an analogy to the three colors in optics. Like the electric charge in QED, each color has an opposite, ?negative? value, carried by the antiquarks, referred to as anti-red (r), anti-green (g),

and anti-blue(b).

1.3 Heavy Ion Collisions

The idea of hot hadronic matter was developed in the early 1950s by various physicists including Enrico Fermi [?]. This concept of applying statistical and hydrodynamical models to a strongly interacting particle ensemble ultimately evolved into the theory of QGP (Quark Gluon Plasma). Since then, systematic studies of hot hadronic matter systems have produced a greater understanding of the state of matter hypothesized to be QGP. QGP has been roughly mapped out in the hadronic phase diagram. The state of matter created in our laboratories is understood to be comparable to the universe about one microsecond after the big bang. And the evolution of the medium has been mapped from the initial heavy ion collision all the way to the final state particles.

Here is the timeline overview of heavy ion collisions in general: At the moment when heavy ions collide relativistically ($\tau=0$), they are length contracted down to flat disks in the lab frame as seen in Figure Then, the initial geometry resulting from the shape of the collision overlap region and fluctuations within the nuclei is transformed into the initial energy density of the medium ($\tau \approx 1 \text{ fm}/c$). At that moment, the hot hadronic matter is thought to be made up of deconfined quarks and gluons in thermal equilibrium, otherwise known as QGP. The system then evolves hydrodynamically, expanding along the pressure gradients present in the initial energy density. At a certain point during this expansion, the medium has cooled down enough in order to form baryons and mesons out of the quark gluon soup in a process known as hadronization. It is important to note that the medium is still in thermal equilibrium at this point but it is no longer known as QGP but instead as hadron gas. Once the medium has cooled down and expanded sufficiently, kinetic freeze-out occurs and the hadron gas becomes a group of particles which have ceased self-interaction ($\tau \approx 10 \text{ fm}/c$). It is this group of final state particles which can be detected much later ($\tau \approx 10^{15} \text{ fm}/c$). Although detectable particles escape the medium at all times, the vast majority of particles we detect are produced at kinetic freeze-out.

Although the field of high-energy nuclear physics is still evolving, several measured properties

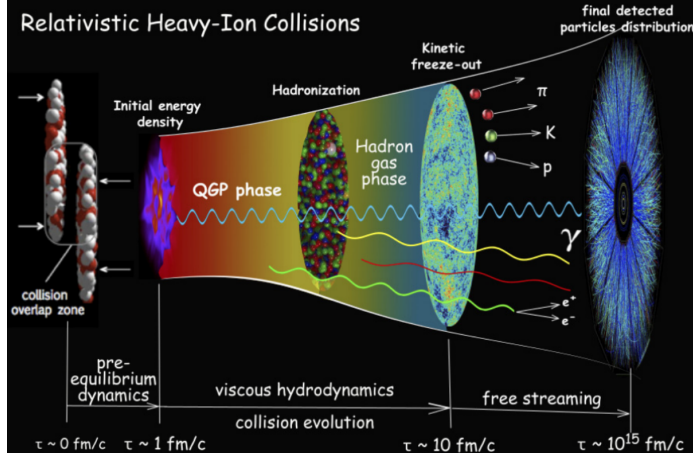


Figure 1.1: TBA

of this state of matter have come together to make QGP the prevailing explanation. Among the best observations indicating QGP are jet quenching, J/ψ melting, and elliptic flow. The observation of jets measured at much lower energies than expected imply that the jets are experiencing energy loss when interacting with a strongly coupled medium. The observation of a severe reduction in the number of expected J/ψ particles matches a prediction that a strongly coupled medium with a temperature above the Hagedorn temperature will melt J/ψ particles. Finally, an elliptic symmetry in the angular distribution of final state particles when viewed along the beam line has been observed. The translation of initial geometry into long-range angular correlations indicates collectivity in a strongly coupled medium.

Chapter 2

Collectivity in QCD

2.1 Conceptual Understanding of Flow

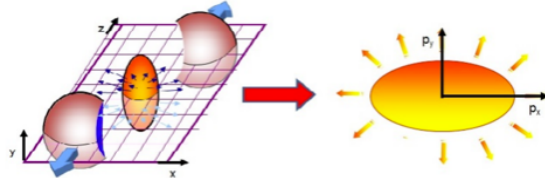


Figure 2.1: TBA

2.2 Mathematical Introduction

A measurement of the azimuthal anisotropy is a way to quantify the extent of long-range angular correlation present in the medium evolution. One way to study the azimuthal anisotropy is to create a correlation function. The 2-particle correlation function method uses pairs of particles from the event in order to create a correlation function. For each pair in an event, a $\Delta\phi$ value is obtained which makes up the signal $S(\Delta\phi, p_T)$. In order to correct for artificial correlations which would distort the distribution from detector effects or other sources, a mixed event background distribution $M(\Delta\phi, p_T)$ is created. The correlation function can be defined as follows:

$$S(\Delta\phi, p_T) = \frac{d(w_{\text{PMT}} N_{\text{Same event}}^{\text{track}(p_T)-\text{PMT}})}{d\Delta\phi}, \quad (2.1)$$

$$C(\Delta\phi, p_T) = \frac{S(\Delta\phi, p_T)}{M(\Delta\phi, p_T)} \frac{\int_0^{2\pi} M(\Delta\phi, p_T) d\Delta\phi}{\int_0^{2\pi} S(\Delta\phi, p_T) d\Delta\phi}. \quad (2.2)$$

Substantial variations in this $C(\Delta\phi, p_T)$ are usually seen as long-range angular correlations which can be attributed to collectivity.

In order to quantify the azimuthal anisotropy, $C(\Delta\phi, p_T)$ is Fourier transformed:

$$C(\Delta\phi, p_T) \propto 1 + \sum_{n=1} 2v_n \cos(n[\phi(p_T) - \Psi_n]) \quad (2.3)$$

where Ψ_n is the event plane angle, ϕ is the azimuth of tracks from the event, and v_n are flow coefficients. The measured v_n averaged over a single event is defined as:

$$v_n = \frac{\langle \cos(n[\phi - \Psi_n]) \rangle}{Res(\Psi_n)} \quad (2.4)$$

where $Res(\Psi_n)$ is the event plane resolution for each event. v_N are further averaged over each event.

$$\varepsilon_n = \frac{\sqrt{\langle r^2 \cos(n\phi) \rangle^2 + \langle r^2 \sin(n\phi) \rangle^2}}{\langle r^2 \rangle} \quad (2.5)$$

2.3 A Review of Flow Measurements in Heavy Ion Collisions

2.4 Collectivity in Small QCD Systems

Small collision systems have been considered too small to create hot and dense matter. These systems were thought to be control experiments which could be used to measure cold nuclear matter effects. However, evidence of collectivity has recently been observed at RHIC in p+Au collisions at $\sqrt{s_{NN}} = 200$ GeV in the most central collisions [3]. Although, the p_T dependent v_N has been measured, what has not been measured in these small systems is the degree to which v_N changes a function of rapidity. This is a particularly interesting measurement to make in an asymmetric collision system such as p+Au.

Recent analyses of d+Au and HeAu collisions at $\sqrt{n} = 200$ GeV [?, ?, ?, ?] at the Relativistic Heavy-Ion Collider (RHIC), and p+Pb at $\sqrt{n} = 5.02$ TeV, and $p+p$ collisions at $\sqrt{n} = 2.76, 5.02, 7,$ and 13 TeV [?, ?, ?, ?, ?, ?, ?, ?] at the Large Hadron Collider (LHC) have demonstrated the existence of the same kind of azimuthal anisotropy signals commonly interpreted as evidence of collective behavior in larger systems. Notably, a feature known as *the ridge* has been observed, consisting of a near-side (i.e., at small relative azimuth) enhancement in the long-range (i.e., at large relative pseudorapidity) azimuthal two-particle correlation. From these correlations, substantial elliptic (v_2), and triangular (v_3) flow coefficients have been measured in these systems.

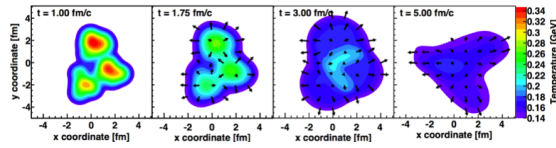


Figure 2.2: TBA

2.4.1 Monte-Carlo Initial Condition Characterization

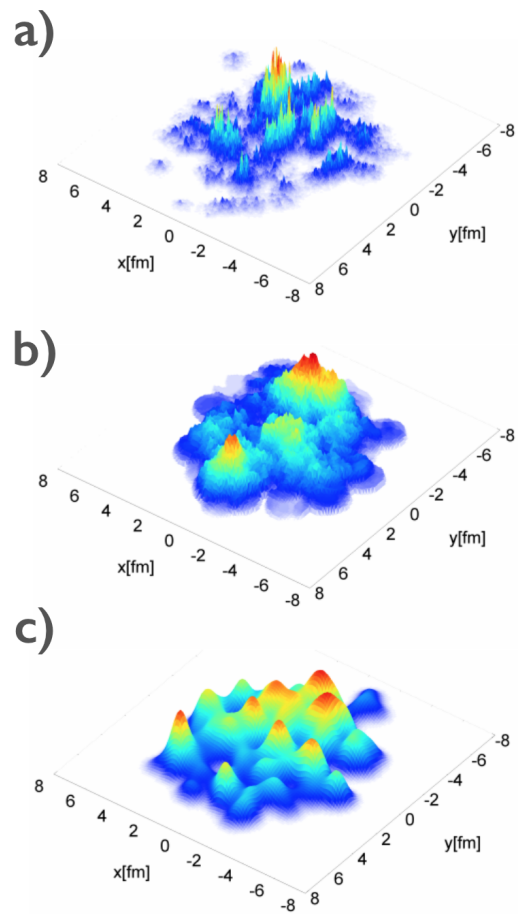


Figure 2.3: a) IP-glasma. b) MC-KLN. c) MC-Glauber.

Chapter 3

Experimental Setup

3.1 RHIC

The Relativistic Heavy Ion Collider (RHIC) is a superconducting charged hadron collider located at Brookhaven National Labs (BNL) in Upton, NY, United States. RHIC is capable of accelerating heavy ions such as Au (gold) or Cu (copper) nuclei to energies of 200 GeV per nucleon. RHIC is also capable of accelerating lighter ions such as protons, deuteron, and helium to 200 GeV per nucleon and 510 GeV per nucleon in the case of protons. The machine has been demonstrated to reliably create so called QGP matter at temperatures in excess of seven trillion degrees Fahrenheit.

There are two major detector experiments currently operating in interaction regions around the RHIC ring: PHENIX and STAR. A typical operation schedule for RHIC is to run the accelerator for five and a half months every year in what is called a "Run". There have been 16 "Runs" so far but the relevant run for this thesis was Run 15 taken in 2015 which ran proton colliding with gold ions (p+Au) at 200 GeV per nucleon for part of its running.

RHIC is at the end of a chain of smaller accelerators that are used to "feed" the ions into RHIC, where they are accelerated (or decelerated in some circumstances) to the desired collision energy. For heavy ions such as Au, the process is listed in detail below [9]. TO DO modify to included EBIS instead of Tandem!

- (1) A pulsed sputter Au ion source generates negative ions in the Tandem Van De Graaff.
- (2) The ions are passed through an electron stripping foil to achieve a positive 12 charge and

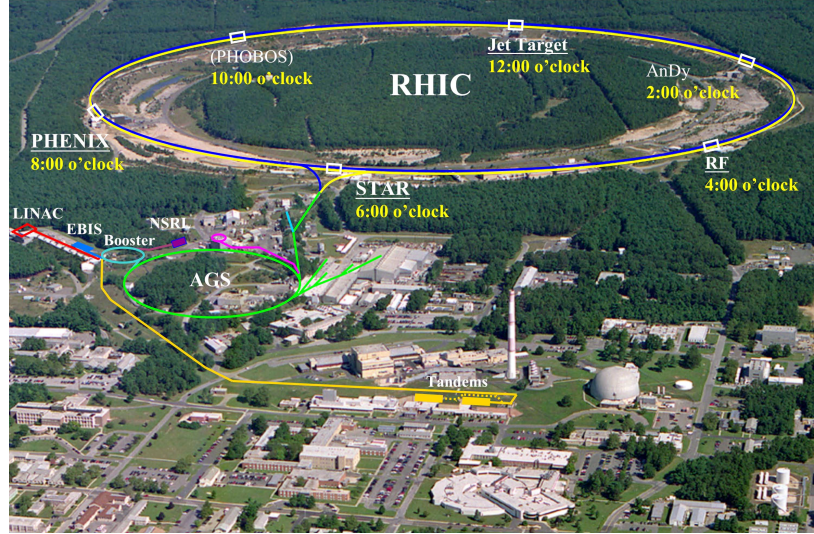


Figure 3.1: A helicopter's view of the accelerator chain in BNL starting at the Tandems (in gold) and ending at the RHIC ring (in blue). STAR and PHENIX can be seen at two of the interaction regions. The ring is 2.38 miles in length.

accelerated to 1 MeV per nucleon.

- (3) The ions pass through magnets to further strip electrons and filter charge, yielding to a positive 32 charge state.
- (4) The ions are sent to the Booster Synchrotron which accelerates them to 95 MeV per nucleon and leaves them at a positive 77 charge.
- (5) The ions enter the Alternating Gradient Synchrotron (AGS) in 24-ion bunches. The ions are debunched and rebunched into four bunches and then accelerated to 10.8 GeV per nucleon.
- (6) The bunches then exit the AGS one at a time, where their Au ions are stripped of their two remaining electrons, yielding a final charge state of positive 79. Finally, the bunches are transferred to their respective buckets in RHIC .

For protons, the process instead begins at the the Linear Accelerator (LINAC) facility. The protons are then sent through the chain of accelerators in a similar way to the heavy ions until

reaching RHIC in either a polarized or unpolarized state.

Once the ions have reached RHIC, they will enter one of two independent rings, blue or yellow, each circulating in an opposite direction. The ions in the rings are deflected and focused by 1,740 superconducting magnets using niobium-titanium conductors. Once the ions are focused and accelerated to the desired parameters around the RHIC, the ions are deflected into the six interactions regions where the blue and yellow rings intersect to produce collisions. It is at these interaction regions where the major experiments have set up their detectors, with STAR at the 6 o'clock position and PHENIX at the 8 o'clock position.

The time period of which the collisions continue is known as a fill, and the average length of a fill is eight hours. As the fill wears on, the collision rate substantially decreases as the density of ions in the machine decreases. Once the collision rate has been reduced sufficiently, it is more cost efficient to start the fill over at a higher collision rate.

For this thesis, the relevant dataset is p+Au 200 GeV Run 15 taken in 2015. Specific details about this dataset are found in section 3.2.4.

3.2 PHENIX

PHENIX, the Pioneering High Energy Nuclear Interaction eXperiment, came online in 2000 along with RHIC and is located at the 8 o'clock interaction region along the RHIC ring. PHENIX is one of the two major RHIC experiments along with STAR, the Solenoidal Tracker At RHIC. PHENIX detector philosophy differs from STAR in that PHENIX makes use of more than a dozen independent detector subsystems of roughly equal experimental weight whereas STAR makes use of only four with its Time Projection Chamber (TPC) being the primary detector.

PHENIX's detectors throughout the years include (in no particular order) the Drift Chamber (DC), the Pad Chambers (PC), the Ring Imaging Cherenkov (RICH), the Hadron Blind Detector (HBD), the Time Expansion Chamber (TEC), the Time of Flight (TOF), the Electromagnetic Calorimeter (EMCAL), the Muon Tracker (MuTr), the Muon Identifier (MuID), the Muon Piston Calorimeter (MPC), the Muon Piston Calorimeter Extension (MPC-EX), the Beam-Beam Counter

(BBC), the Zero Degree Calorimeter (ZDC), the Forward Calorimeter (FCAL), the Multiplicity and Vertex Detector (MVD), the Reaction Plane Detector (RPD), the Resistive Plate Chambers (RPC), the Silicon Vertex Detector (VTX), and the Forward Silicon Vertex Detector (FVTX). For this thesis, the relevant detectors installed in 2015 are the DC, PC, RICH, BBC, and FVTX. The DC, PC, and RICH are located in the mid-rapidity region relative to collisions (Central Arms) and the BBC and FVTX are located in the forward (and backward) rapidity region relative to collisions (Forward Arms) [5].

PHENIX makes use of the three powerful magnets in order to bend charged the particles' trajectories: the Central Magnet (CM), the North Muon Magnet (MMN), and the South Muon Magnet (MMS). For this thesis, the relevant magnet is the CM.

PHENIX makes use of a state of the art Data Acquisition System (DAQ) which is capable of writing 400 MB/s of information to disk. More details about the PHENIX DAQ are found in section 3.2.3.

3.2.1 Forward Rapidity Detectors

3.2.1.1 Beam Beam Counter

The BBC is a forward detector used to determine the event start time, vertex, centrality, and event plane. The BBC is composed of two mirror image arrays, a South and a North Arm, that surround the beam pipe 144 cm on opposite sides of the nominal collision point just behind the Central Magnet, covering $3.0 < |\eta| < 3.9$ and 2π radians in azimuth. Each BBC arm is made of 64 elements each composed of a 3-cm length quartz Cherenkov radiator connected to a 2.5 cm diameter Hamamatsu R6178 mesh dynode PMT (photomultiplier tube), as shown in Fig 3.4. The outer and inner diameters of the BBC are 30 cm and 10 cm, respectively.

The BBC has a timing resolution of 524 ps. The BBC is used to mark the event start time for the entire PHENIX detector by averaging the emitted particles arrival time at each BBC arm.

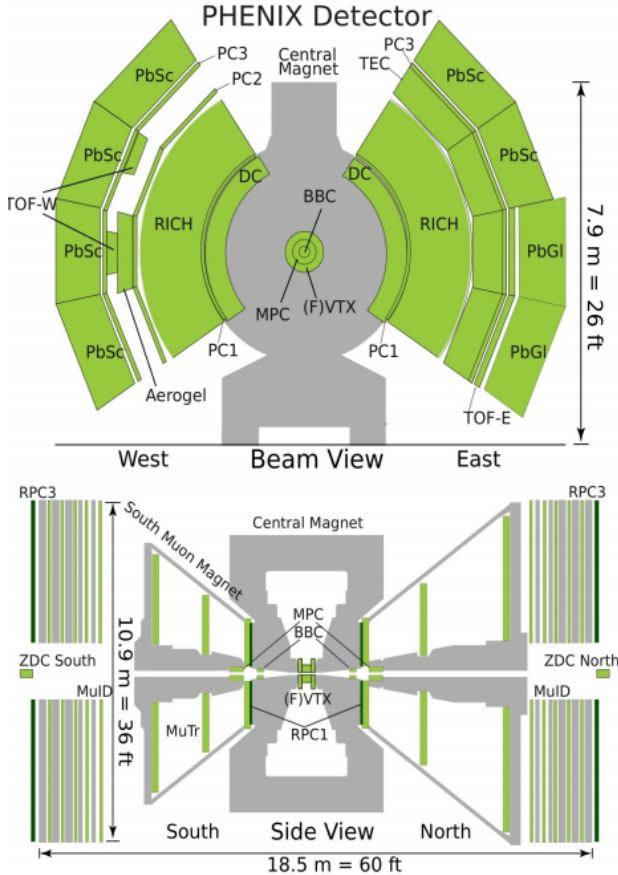


Figure 3.2: The top is a cross section diagram of the PHENIX detector from the incoming beam's perspective. The bottom is a cross section diagram of the PHENIX detector from the top down. The central arm detectors are not present in the bottom diagram.

The timing difference between each arm provides an estimate of the collision's z-vertex by

$$z = c \frac{T_S - T_N}{2}, \quad (3.1)$$

where T_S, T_N are the particle's arrival times for each arm and c is the speed of light. In typical Au+Au 200 GeV collisions the BBC z-vertex resolution is 0.5 cm. This rough estimate of the vertex is used during triggering. Specific details about triggers are in section 3.2.3.

3.2.1.2 Forward Vertex Detector

The FVTX is a PHENIX detector upgrade which became operational for physics data taking in 2012. The FVTX uses include charged particle tracking, collision vertex determination, and

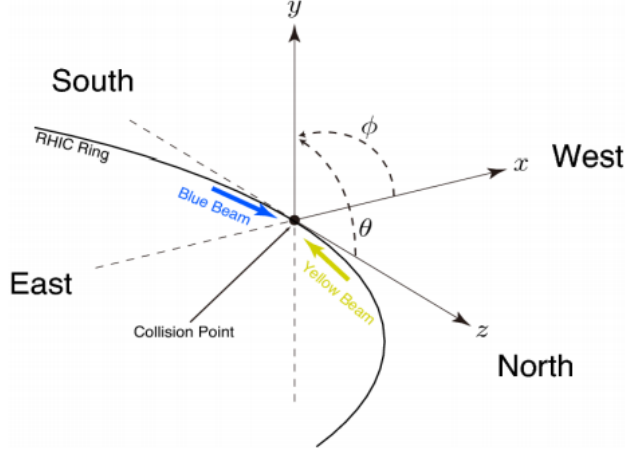


Figure 3.3: The PHENIX coordinate system. The origin is in the middle of the PHENIX detector at the collision point. North and south are parallel to beam axis. East and west are transverse to the beam axis. Central detectors have a west and an east arm on either side of the beam. Forward detectors have a north and a south arm relative to the origin.

event plane determination [4]. The FVTX consists of two identical endcaps covering a combined pseudorapidity range of $1 < |\eta| < 3$ and full azimuth coverage. Each endcap has four stations of silicon mini-strip sensors with a pitch of $75 \mu\text{m}$ arranged in the radial direction around the beam pipe. The basic unit of construction is a wedge that has a silicon strip sensor and read-out chips. There are four FVTX layers in each endcap.

3.2.2 Midrapidity Detectors

3.2.2.1 Drift Chamber

The DC consists of two gas multi-wire chambers, one located in each arm. The DC is used to measure particle trajectories in the $r \phi$ plane. The DC is the innermost subsystem in the central arms, located 2 m from the z-axis, placing it in a residual magnetic field of 0.6 kiloGauss from the CM. Apart from the VTX, the DC is the first detector encountered by a particle in mid-rapidity.

As a charged particle passes through the DC volume, the gases are ionized to create free electrons. These electrons cause a chain reaction of ionizations which are measured by an anode wire. The DC is designed in such a way that the drift velocities of the electrons are predictable

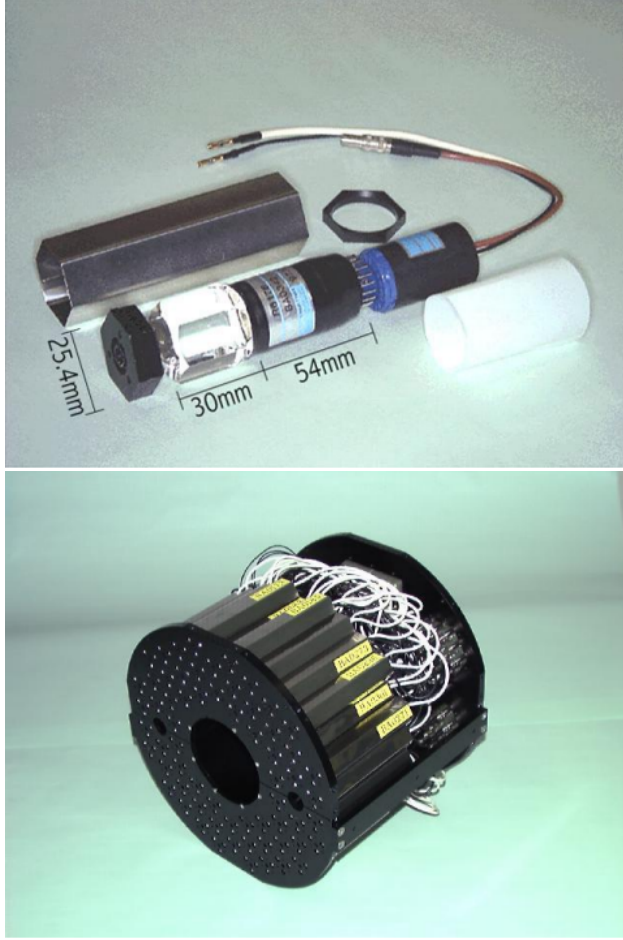


Figure 3.4: Photographs of the BBC detector. The left is of a single detector element consisting of a quartz Cherenkov and a PMT. The right is of one of the BBC arms, consisting of 64 detector elements.

enough to relate time and position together.

Each identical DC arm is cylindrical in design and covers 2.5 m along the beam direction and is 0.4 m thick as seen Fig 3.6. A gas mixture of 50% Argon and 50% Ethane is used in each arm of the DC. Each arm is divided into 20 equal sectors covering 4.5 degrees in ϕ . Each sector contains six types of wire modules stacked radially and labeled X1, U1, V1, X2, U2, V2, respectively from the inside out. The X wires run parallel to the beam to perform precise four ϕ measurements while the U and V wires are set at small angles of about six degrees relative to the X wires to provide information about the z position of the track. A diagram of the wire layout in each sector is shown

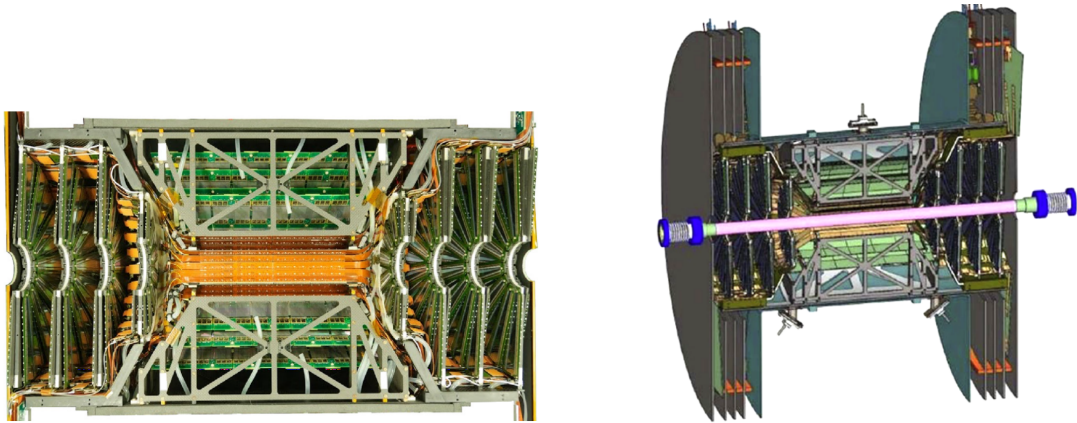


Figure 3.5: The left is a photograph of half of the FVTX. The FVTX are the half disks on either end of the picture. The FVTX is only 20 cm in the z direction from the PHENIX coordinate system origin (the center of the picture. The right is a schematic of the FVTX at a slightly different angle.

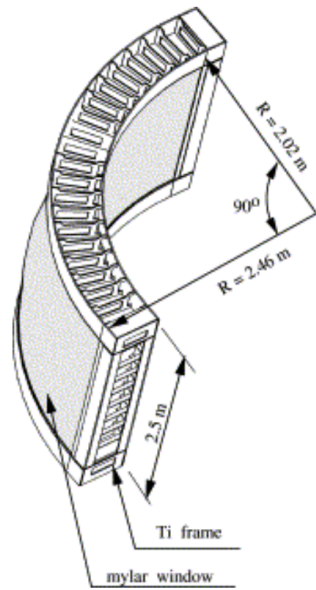


Figure 3.6: A diagram of the DC titanium frame which encloses the detector.

in Figure 3.7. In total, the DC consists of 6500 anode wires leading to 13,000 readout channels, with a measured single wire resolution of 165 m and a spatial resolution of 2 mm.

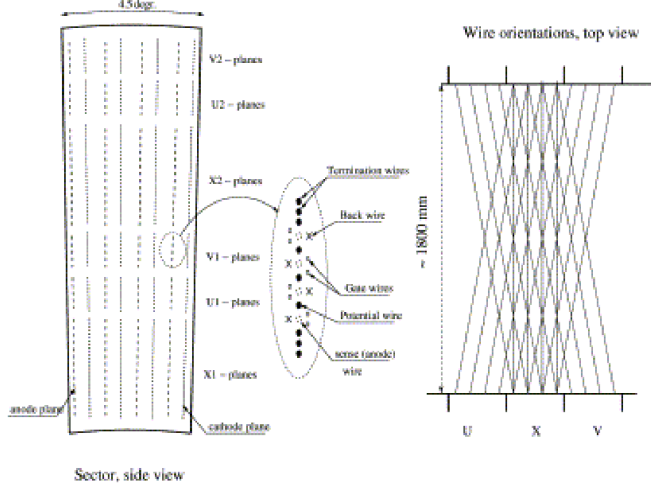


Figure 3.7: A diagram of the X, U, and V wires in the DC.

3.2.2.2 Pad Chambers

The PCs are multi-wire proportional chambers which consist of three separate layers of detectors measuring precise hit positions and making up the bulk of the PHENIX tracking system. The innermost layer, PC1, is located in both the East and West arms immediately outside the DC, providing a measurement of the z position at the back plane of the DC. The second layer, PC2, is located behind the RICH in the West arm only. The outer layer, PC3, is in both arms and provides a second point on the straight line trajectories of the tracks through the detector, outside of the magnetic field.

3.2.2.3 Ring Imaging Cherenkov Detector

The RICH detector is located immediately behind the PC1 and provides the primary electron identification for PHENIX. The RICH consists of two identical detectors located in each arm and provides e over π discrimination below the pion Cherenkov threshold of 4.65 GeVc in the CO₂ gas used in the detectors.

3.2.2.4 Electromagnetic Calorimeter

The EMCAL is the outermost subsystem in the central arms and is designed primarily to measure the energies and positions of photons and electrons. It also plays a key role in the identification of as well as providing triggering for rare events. Two different EMCAL designs were utilized with 6 sectors based on a lead-scintillator design and 2 sectors based on a lead-glass design. The two different designs were chosen deliberately as each provides advantages and disadvantages, for instance the lead glass has a better energy resolution, while the lead scintillator has better linearity and timing.

3.2.3 PHENIX Data Acquisition System

PHENIX makes use of a fast DAQ to manage the transfer and collation of hundreds of kB of event data from over two dozen independent detector subsystems at a rate of over 6 kHz. This amounts to writing to disk hundreds of MB/s, something which the PHENIX DAQ consistently achieves for months of around the clock use.

The collection of a Granule Timing Module (GTM), Front End Modules (FEM), and a Data Collection Modules (DCM) is known as a granule and is the minimal combination of DAQ hardware sufficient for data production as shown in Fig 3.2.3.1. Each detector subsystem's output data is managed by a granule. Pipelined Field ProGrammable Arrays (FPGA) with carefully controlled dead time are used to calculate the trigger decisions. The FPGAs are fed information from the experiment. Once the FPGAs compute the trigger decision, the trigger signals are monitored by the GTM. If trigger decision is positive, the GTMs instruct the FEMs to release their data from their buffers and send them to their graunules' DCM. If the decision is negative, otherwise the FEMs are instructed to dump the data. Once the DCM is instructed to send its data downstream, it is sent to the event builder which will be discussed in an upcoming section.

3.2.3.1 Triggering

PHENIX has the capability of running 128 independent triggers, in practice only 32 are used. Each of the triggers have a scale down number to control the relative bandwidth each trigger receives. To understand the PHENIX triggers, it is useful to learn about the beam clock.

The PHENIX trigger is tied to the clock of the blue beam, one of the two counter circulating rings of which RHIC is comprised. The clock rate is fixed at 9.38 MHz and is tied to the rate at which RHIC overlaps bunches of ions in the interaction regions. Every time a bunch of ions from the blue ring overlap with a bunch of ions from the yellow ring, there is a blue clock trigger. This clock is stable by necessity of the precision required to run a complex accelerator like RHIC. This blue clock trigger is the backbone of PHENIX triggering for there can be no ion collision event if there is no overlap of bunches. Consequently, almost every PHENIX trigger is AND'd with the clock trigger.

The trigger which is given the largest bandwidth is the minimum bias (minbias) trigger. As the name suggests, the trigger seeks to mark the detection of an ion collision while reducing the any bias to the type of the collision to a minimum. To achieve this, data from the BBC and ZDC are used, although the ZDC is less relevant than the BBC for defining the trigger. Although what constitutes a minbias observation varies with collision species, the BBC minbias trigger is generally defined as >0 PMTs in each arm above threshold. Not only is this condition a good indication that a ion collision occurred, it is also the minimum information necessary to calculate the collision vertex position using the BBC. The vertex information is important because it is used to select for collisions which occur in the narrow range of acceptance of current PHENIX detector configuration. This range is $-10 \text{ cm} < z < 10 \text{ cm}$ where z is defined in the PHENIX coordinate system in fig (TBA). For completeness, PHENIX takes BBC minbias triggers with z vertex cuts of 30 cm and with no vertex cut. The collection of all these triggers is what is considered to be the PHENIX minbias trigger.

In Run 15, a unique high multiplicity trigger was implemented to enhance event statistics for

events producing the most amount of particles. This trigger consisted of requiring at least 35 out of 64 PMTs in the south arm of the BBC. More details about this trigger are located in section 3.2.4.

Table 3.1: An example Run15 p+Au 200 GeV relevant trigger configuration and parameters. A trigger's scale down number reduces its rate by $1/(1+\text{scale down})$.

<i>Trigger Name</i>	<i>Scale down</i>	<i>Trigger rate</i>	<i>Vertex cut</i>	<i>Part of minbias</i>
<i>Clock</i>	196077	45Hz	<i>N/A</i>	<i>no</i>
<i>BBC(> 0 PMTs)</i>	100	695Hz	10cm	<i>yes</i>
<i>BBC(> 0 PMTs)</i>	2083	88Hz	30cm	<i>yes</i>
<i>BBC(> 0 PMTs)</i>	3959	94Hz	<i>no cut</i>	<i>yes</i>
<i>BBC(> 35 PMTs)</i>	1	1640Hz	10cm	<i>no</i>

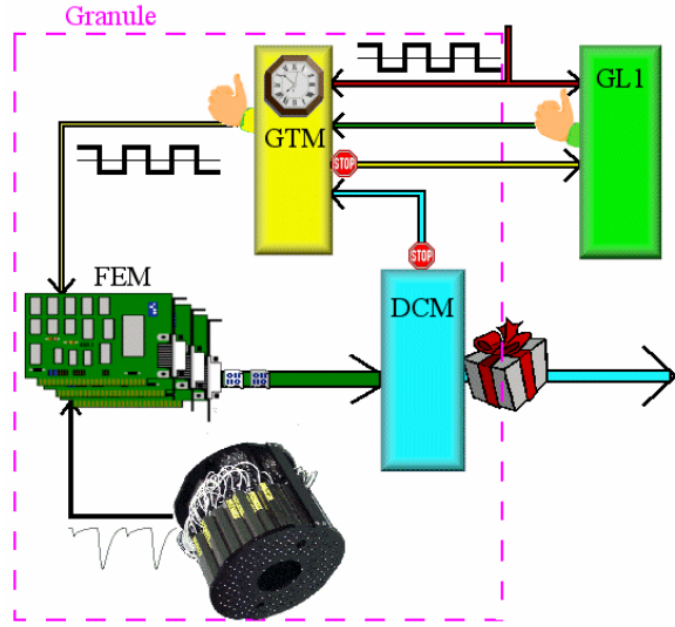


Figure 3.8: Diagram of a granule. Granules are the building blocks of the PHENIX DAQ. Each detector subsystem has at least one granule.

3.2.3.2 Event Builder

Following the PHENIX DAQ downstream, after a positive trigger decision has been sent to each of the granules, the granules' data packets are sent to the event builder. It is the event

builder's job to associate each granule's data packet from the same collision event into one bundle of data known as an event. The event builder consists of Sub Event Buffers (SEB), Assembly Trigger Processors (ATP), an Event Builder Controller (EBC), and a Gigabit Ethernet Switch as the communication management. Fig 3.9 provides a diagram of how these components are connected.

Granules send the data packets to the specific SEB assigned to that granule. The EBC receives global trigger information and assigns each ATP a specific collision event. The ATP then requests the data from all of the SEBs for the specific event assigned to it by the EBC. Once the ATP is successful, it writes the assembled event to disk and the EBC instructs the SEBs to flush the buffer for that event.

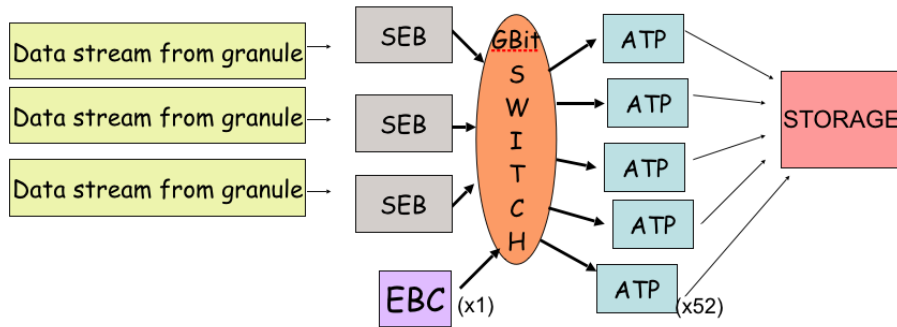


Figure 3.9: Diagram of the event builder.

3.2.4 Run 15

Run 15 is the RHIC running period in the year 2015 which marks fifteen consecutive years of RHIC running since the year 2000. Run 15 began in January 2015 and ended in June of 2015. There were approximately eleven weeks of research viable, polarized p+p collisions at $\sqrt{s} = 200$ GeV, approximately 5 weeks of research viable polarized p+Au collisions at $\sqrt{s} = 200$ GeV, and approximately one week of research viable p+Al collisions $\sqrt{s} = 200$ GeV. Of interest to this thesis are the p+p and p+Au datasets.

In addition to providing the min-bias trigger for Run 15, the BBC was used to implement a

Table 3.2: Some relevant RHIC parameters from Run 15.

Collision Species	p+p	p+Au	units
Total Particle Energy	100.2	$103.9 + 100.0$	GeV/nucleon
Ions per Bunch	225	$225 + 1.6$	number $\times 10^9$
Number of Bunches	111	111	number
Luminosity Average Per Fill	63×10^{30}	45×10^{28}	$cm^{-2}s^{-1}$
Total Delivered Luminosity	382	1.27	pb^{-1}
Average Fill Lifetime	8	7	hours

high-multiplicity trigger in order to enhance the amount of the top 5% highest multiplicity events. The high-multiplicity trigger requires 35 of the 64 BBC south arm PMTs to be above threshold in a given event to be satisfied. The relevant BBC arm for p+Au is the south arm since that is the Au-going direction so the multiplicity is much higher in the south arm. The enhancement can be seen in Figure 3.10.

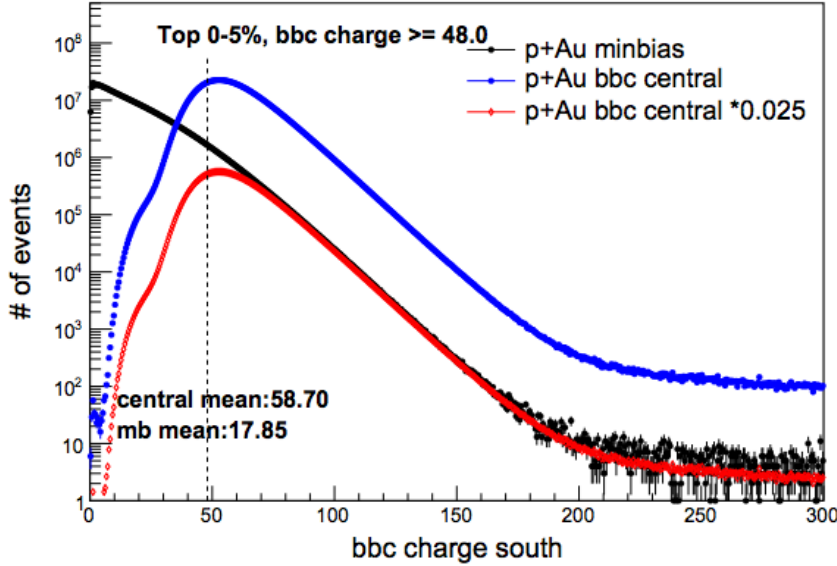


Figure 3.10: The distribution of BBC charges in p+Au 200 GeV events for different triggers. The black curve is the distribution of charges for the minbias trigger. The blue and red curves are the distributions of charges for the high multiplicity trigger. The red curve being scaled by a factor of 1/40 to show agreement with the black curve. The definition of the top 5% more central events are BBC south charges ≥ 48.0 . The plot shows the large enhancement of the number of 0-5% centrality events that are gained using the high multiplicity trigger compared to the number of 0-5% centrality from the minbias trigger alone.

3.2.4.1 Beam Collision Geometry

For Run 15 p+Au 200 GeV running, RHIC's blue and yellow beams were not in perfect accordance to the PHENIX coordinate system. This was manifested in two separate ways. First of all, the collision vertex is significantly offset from the z-axis to which all of the PHENIX detectors are aligned. This is a typical situation in PHENIX datasets but it must be addressed. The other effect, and the more significant of the two, comes from the fact that the beams are colliding at an angle of 3.6 milli-Radians in the x-z plane as illustrated in Fig 3.11. This is a result of configuring RHIC magnets for the specific charge to mass ratios of the p+Au collision species. The collision vertex in x and y is known as the beam center. The beam center varies over the course of data taking but its values on average are $(x, y) = (0.206, 0.065)(cm)$. The distribution of z-vertices from collision events can be see in Fig 3.12. Due to the fact that the beams are colliding at an angle in the x-z plane, the x-component of the beam center will have a z-vertex dependence with a slope of -0.0036 cm of x per 1 cm of z. Apart from how the beam angle effects the beam center values, it also violates the expectation of a uniform ϕ distribution of particles with respect to PHENIX detectors. PHENIX detectors are designed and aligned with respect to the PHENIX coordinate system with the expectation of geometric symmetry. A significant beam collision angle with respect to PHENIX detectors would be equivalent to PHENIX detectors being tilted which would violate geometric symmetry. The physics analysis described in this thesis is sensitive to these beam geometry effects. A discussion on how to account for these effects will be in chapter 4.

3.2.5 centrality determination

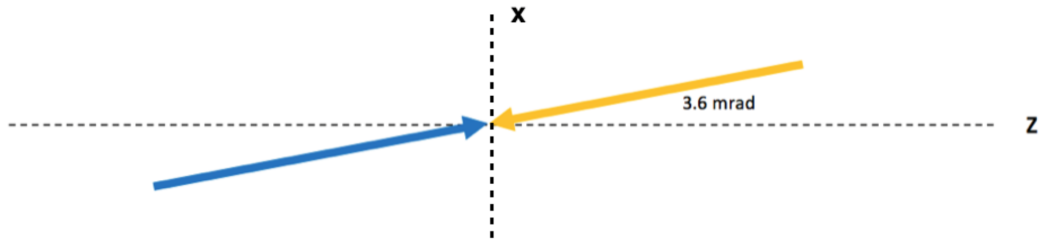


Figure 3.11: A vector diagram illustrating the yellow and blue beam angle confirmation relative to the PHENIX coordinate system.

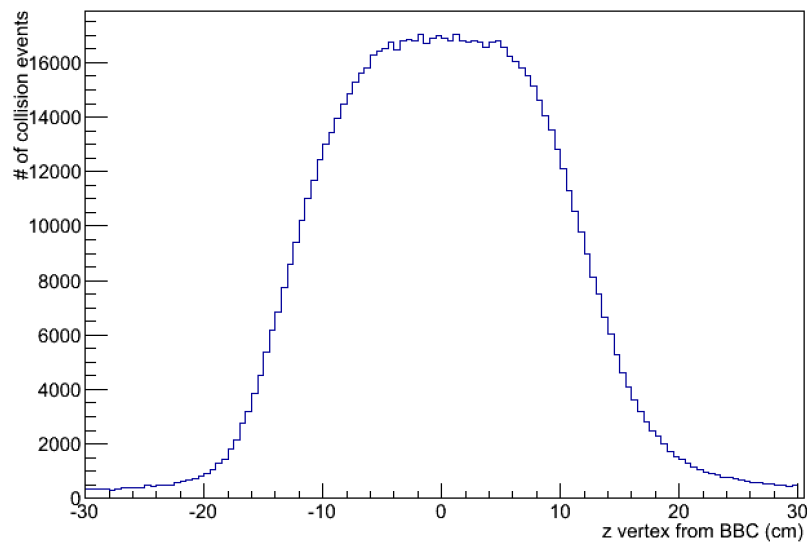


Figure 3.12: The distribution of BBC calculated z-vertex positions for events in p+Au 200 GeV. There are more events between -10 and 10 cm because of the BBC narrow trigger.

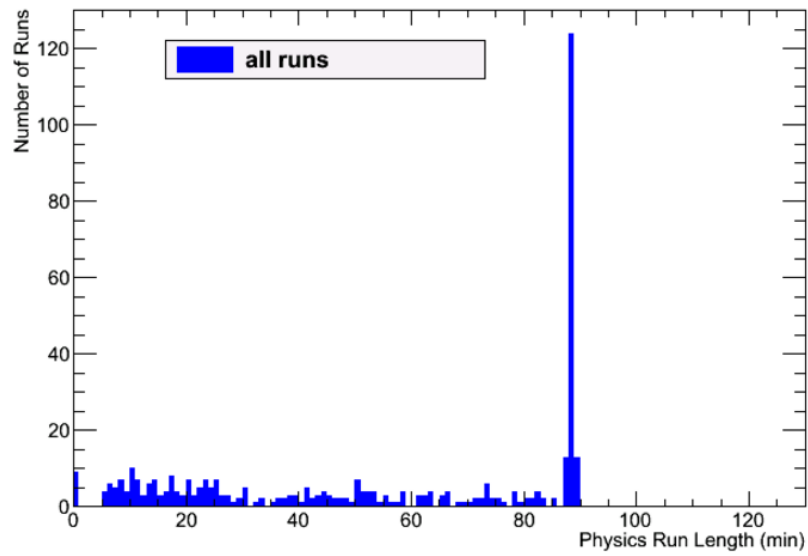


Figure 3.13: The distribution of the length of physics runs.

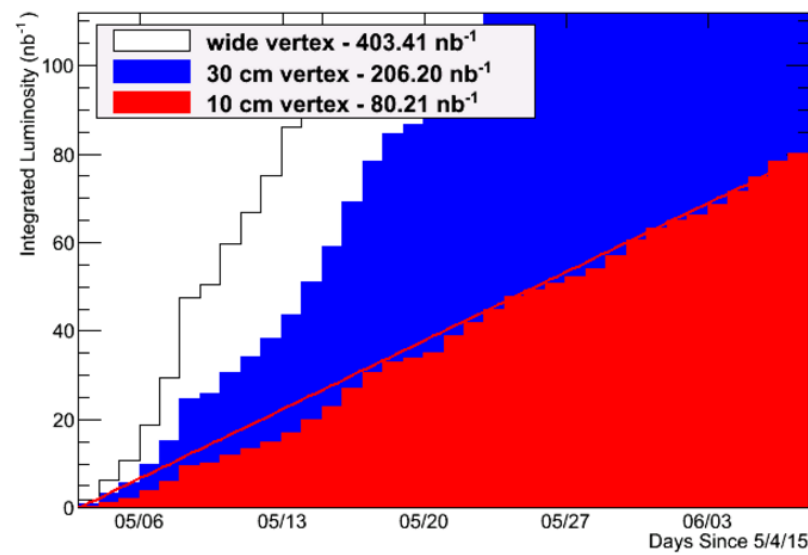


Figure 3.14: Integrated luminosity from the p+Au dataset.

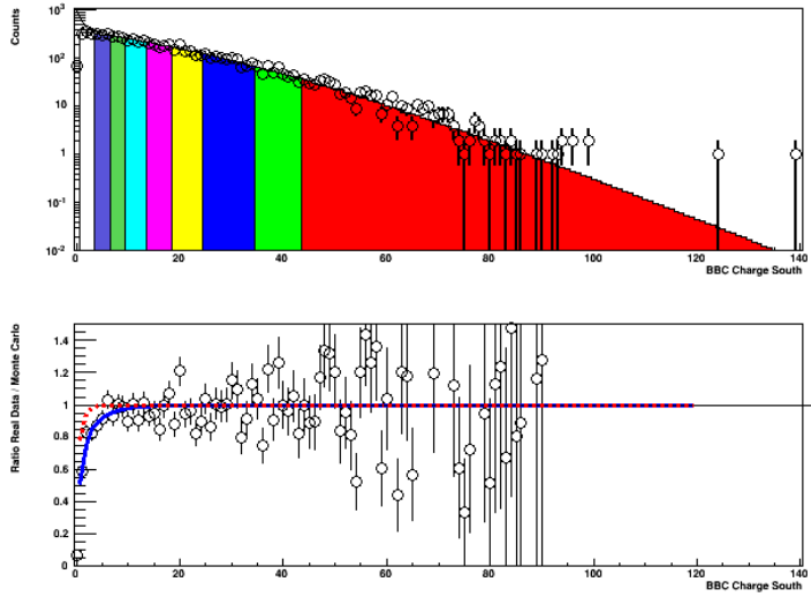


Figure 3.15: Real data for BBC Charge South (Au-going direction) shown as open circles and Glauber Monte Carlo + NBD. The colors correspond to the various percentiles relative to the total inelastic p+Au cross section, the most central 0-5% in solid red. The blue and red curves correspond to the Leve-1 trigger efficiency in all inelastic collisions and inelastic collisions producing a particle at midrapidity, respectively. The best fit NBD parameters are $\mu = 3.14$, $k = 0.47$, and the trigger firing on $84 \pm 3\%$ of the total inelastic cross section [sigma = 1.76 barns].

Chapter 4

Analysis

4.1 Direct Observables: The Building Blocks of the Measurement

In this section, I will be detailing the relevant direct observables used in this measurement. They include parameters from central arm tracks, FVTX clusters, and BBC PMTs. Although the Central Arms, FVTX, and BBC have already been described in chapter 3, I will go into more detail into the parameters available and their mathematical precision.

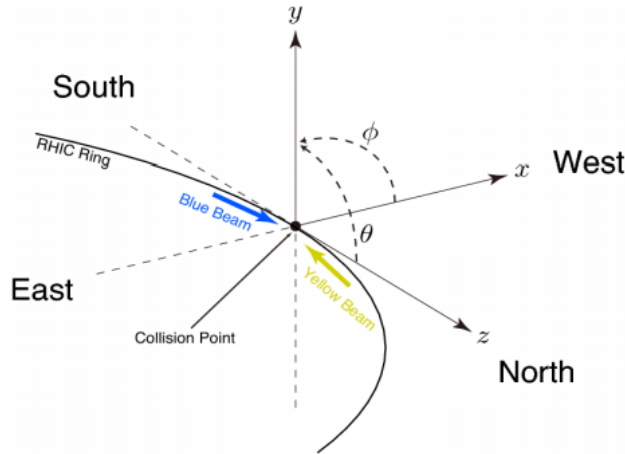


Figure 4.1: For reference, I will show the PHENIX coordinate system here. The origin is in the middle of the PHENIX detector at the collision point. North and south are parallel to beam axis. East and west are transverse to the beam axis. Central detectors have a west and an east arm on either side of the beam. Forward detectors have a north and a south arm relative to the origin.

4.1.1 Central Arm Tracks

This analysis uses central arm tracks. A central arm track is a charged particle emitted from the heavy ion collision and detected by the PHENIX central arms. There are 2 central arms and each one covers $\eta < |0.35|$ and $\frac{\pi}{2}$ in azimuth. The drift chamber provides momentum information and the pad chambers provide track quality metrics. The RICH provides electron identification.

One of the physical parameters of central arm tracks relevant to this analysis is the momentum vector: $p = (p_x, p_y, p_z)$ defined at the collision vertex. CNT have a good momentum resolution as seen in Fig 4.6. The momentum components are used to calculate the azimuthal angle ϕ and the psuedo-rapidity η . The momentum range of the CA tracks used in this analysis is from 0.02 - 3.5 GeV/c.

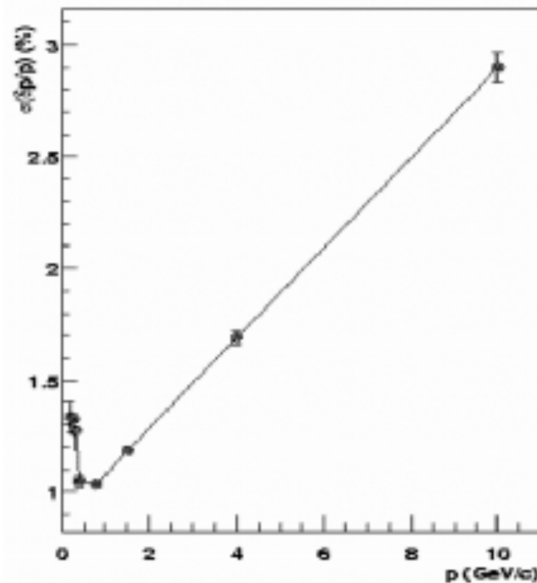


Figure 4.2: Momentum resolution $|p_{reco} - p_{gen}|/p_{gen}$ (in percent) as a function of p_{reco} where p_{reco} is the reconstructed momentum and p_{gen} is the generated momentum of simulated single particle events [1].

There are also a number of central arm track parameters which are used to ensure the quality of the track sample. These parameters include the pad chamber's sigmalized $d\phi$ and dz , n_0 , and the general track quality. The sigmalization calibration of the pad chamber $d\phi$ and dz parameters

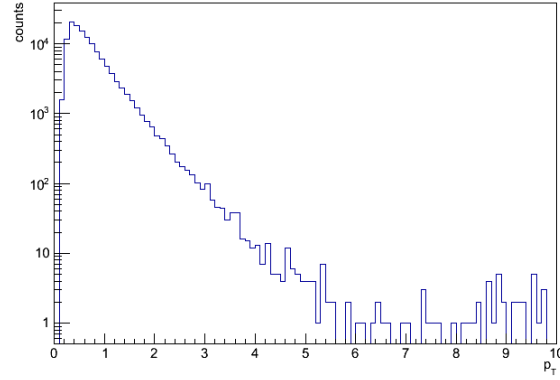


Figure 4.3: The transverse momentum p_T distribution of central arm tracks. This is shown without any cuts. There are some junk tracks at high p_T .

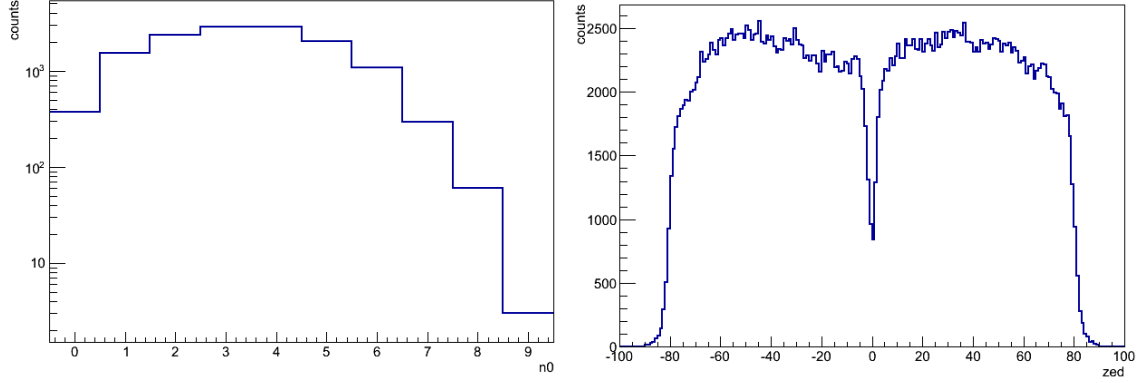


Figure 4.4: The distribution of n_0 (number of PMTs fired in the RICH) is plotted on the left. The zed distribution is plotted on the right. The structure in the zed variable is from the structure of the DC detector.

Table 4.1: DC track quality summary.

Quality	PC1 found	PC1 unique	UV found	UV unique
17,18,19	1	0	0	0
21,22,23	1	0	1	0
29,30,31	1	0	1	1
49,50,51	1	1	1	0
61,62,63	1	1	1	1

is discussed in section 3.5. The n_0 parameter determines whether the charged particle is an electron by counting the number of PMTs fired in the RICH that match the DC track projection. The n_0

and zed parameter distributions can be seen in Fig 4.4 and the p_T distribution can be seen in Fig 4.3. Using these parameters ensures the track sample is a relatively clean collection of charged hadrons.

Table 4.2: Central Arm Track Cuts.

<i>variable</i>	cuts	units
p	$0.02 < p < 10.0$	GeV/c
zed	$ zed < 75$	cm
PC3 $d\phi$	$ d\phi < 2.0$	radians $\times 10^9$
PC3 dz	$ dz < 2.0$	cm
n_0	$n_0 >= 0$	count
quality	63 or 31	N/A

4.1.1.1 Pad Chamber 3 Sigmalization

The goal of PC3 variables is to match the ϕ angle and z-direction coordinate between pad chamber third layer and drift chamber. All the matching procedures are done in minimum bias sample and apply in other trigger samples. We did the matching in different transverse momentum bins and separate east arm or west arm, positive or negative particles. The $d\phi$ and dz distributions are fitted for a double-Gaussian function. Then the parameters are smoothed as a function of p_T . Fig 4.1.1.1 a) shows in $1.0 < p_T < 1.1$ (GeV/c) the matching fit of $d\phi$ distribution in both west arm, east arm and positive and negative charged particles. Fig 4.1.1.1 b) shows in $1.0 < p_T < 1.1$ (GeV/c) the matching fit of dz distribution in both west arm, east arm and positive and negative charged particles. Then we fit the signal Gaussian mean and sigma by some polynomial functions.

Once the mean and sigma are calculated by the smooth fitting. We only keep the particles/tracks within 2σ range.

4.1.2 FVTX Clusters

This analysis uses clusters from the forward vertex detector (FVTX). The FVTX detects charged particles traveling through its silicon layers. The intersection of the charged particle and

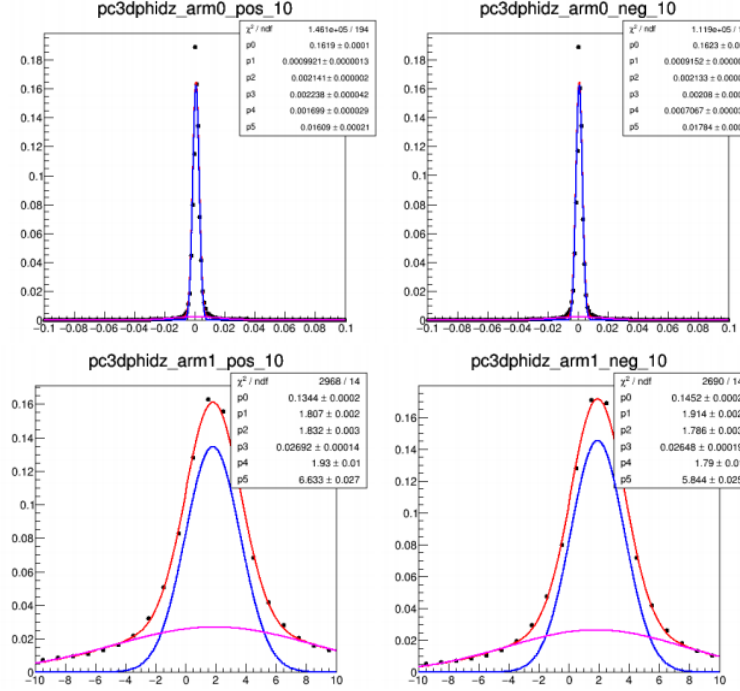


Figure 4.5: The top 2 plots are the PC3 matching $d\phi$ fit in range $1.0 < pT < 1.1$ (GeV/c) as a example. The red line is the fit for the double Gaussian function, the blue line is the signal Gaussian function according to the fit and the pink line is the background Gaussian function. The bottom two plots are the same as the top 2 plots except the PC3 matching dz fit is shown instead.

the FVTX detector is recorded in each of the 4 layers the particle goes through. Each intersection is known as a cluster. Each cluster is expected to be produced from a single charged particle. This assumption is a good one in the p+Au @ 200 GeV dataset because of the low multiplicity. These clusters have a position resolution in x and y (or r and ϕ) of 50 μm and have a z RMS that is the width of the FVTX layer ($\frac{200}{\sqrt{12}}$ μm). The FVTX acceptance is $1 < |\eta| < 3$ and spans the full azimuth [4]. In this analysis, only the clusters from the south arm are used due to the south arm being where most of the particles are from the Au-going direction. In a typical 0-5% central event, there are 1500 FVTX clusters in the south arm alone on average.

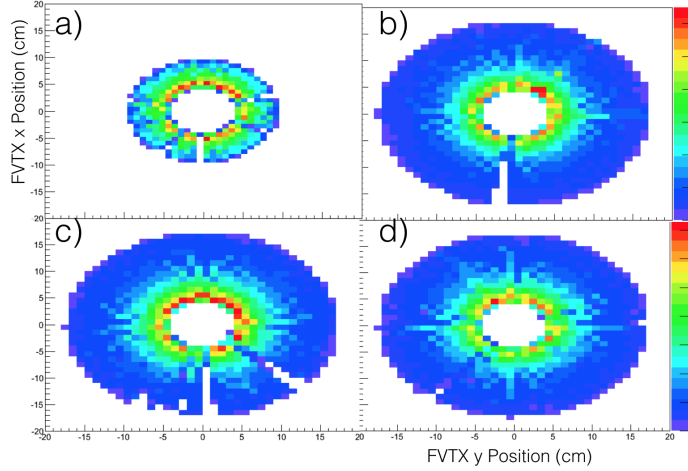


Figure 4.6: The distribution of FVTX clusters in x and y for layers 1, 2, 3, and 4 for panels a), b), c), and d) respectively. The z-axis is counts.

4.1.3 BBC PMTs

This analysis uses photomultipliers (PMTS) from the beam beam counter (BBC). The BBC detects charged particles traveling through its quartz radiator material. The BBC acceptance is $3.1 < |\eta| < 3.9$ and spans the full azimuth. The BBC provides position information in x, y, and z and, like the FVTX, the x and y (r and ϕ) resolution differ from the z resolution in that the z resolution is simply the width of the active area of the BBC. In addition to position information, the BBC provides charge information which is calibrated so that a value of 1.0 corresponds to a single particle signal. Fig 4.7 shows the layout of the PMTs for the BBC. As discussed in section 3.2.1.1, the BBC's direct variables of PMT time and charge can be used to calculate the derived observable of collision z-vertex. This distribution can be seen in Fig 3.12.

In this analysis, the BBC provides charged particle position information at forward rapidity, the z-vertex of the collision, and the centrality class of the event.

4.2 Event Plane Method

The event plane method works by calculating a mathematical object called an event plane angle from the data. This event plane angle is defined for each harmonic and is sometimes denoted

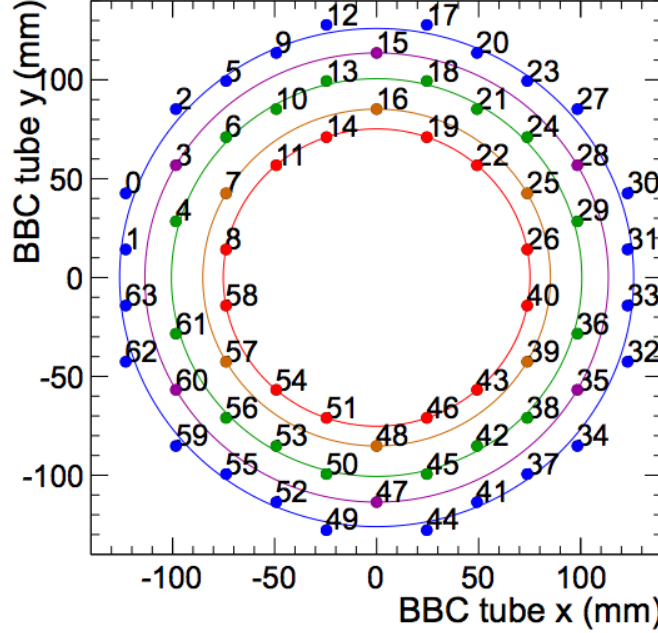


Figure 4.7: A diagram showing the positions of the PMTs for the BBC south detector. Colored rings indicate PMTs at an approximate common radius. Each color indicates a different radius. There are five rings.

as Ψ_n where n is the harmonic number. The definition for Ψ_n is related to the calculation of the Q-vector:

$$Q_x = \sum_i (w_i * \cos(n * \phi_i)) \quad (4.1)$$

$$Q_y = \sum_i (w_i * \sin(n * \phi_i)) \quad (4.2)$$

$$Q_w = \sum_i (w_i) \quad (4.3)$$

$$\Psi_n = \arctan\left(\frac{Q_y}{Q_x}\right), \quad (4.4)$$

where i is the i th component of the detector, ϕ_i is the azimuthal angle of the detector component, w_i is the weight factor, and n is the harmonic number. The Q_w is the length of the Q-vector is only used during the event plane calibration. Once the event plane has been calculated, the flow

harmonics (v_n) are calculated as

$$v_n = \frac{<< \cos(n(\phi - \Psi_n)) >>}{Resolution(\Psi_n)}, \quad (4.5)$$

where $<<>>$ means averaged over all particles in an event and all events [8]. The resolution of Ψ_n is calculated using the 3-subevent method. It is important to note the the set of particles used to calculate Ψ_n and ϕ must be different in order to avoid autocorrelations. This is usually done by imposing an η gap between two particle sets.

For this analysis, the event plane is calculated separately for each of the forward detectors mentioned above, the BBC and the FVTX. For the FVTX, the Q-vector is calculated in each event as

$$Q_x = \sum_i^{NClus} (\cos(n * \phi_i)) \quad (4.6)$$

$$Q_y = \sum_i^{NClus} (\sin(n * \phi_i)) \quad (4.7)$$

$$\phi_i = \arctan\left(\frac{Clus_y^i}{Clus_x^i}\right) \quad (4.8)$$

where NClus is the number FVTX clusters in that event and $Clus_{y,x}^i$ are the x and y components of the i th FVTX Cluster in that event. This Q-vector is calculated with no cluster dependent weight factor as each cluster is taken to be equal weight.

For the BBC, the Q-vector is calculated in each event as

$$Q_x = \sum_i^{NPMT} (w_i \cos(n * \phi_i)) \quad (4.9)$$

$$Q_y = \sum_i^{NPMT} (w_i \sin(n * \phi_i)) \quad (4.10)$$

$$Q_w = \sum_i^{NPMT} (w_i) \quad (4.11)$$

$$\phi_i = \arctan\left(\frac{PMT_y^i}{PMT_x^i}\right) \quad (4.12)$$

where w_i is the charge collected on the PMT and NPMT is the number of PMTs that fired (above threshold) in each event.

Finally, the v_n are calculated using a combination of the BBC or FVTX Q-vectors and the CNT tracks as

$$v_n = \frac{\left\langle \left\langle \cos(n(\phi^{CNT} - \Psi_n^{BBC,FVTX})) \right\rangle \right\rangle}{Resolution(\Psi_n^{BBC,FVTX})}. \quad (4.13)$$

In this analysis, I will be exclusively focusing on the second harmonic v_2 ($n=2$). The reason for this is two-fold:

- (1) The second harmonic is usually the largest and easiest to measure harmonic.
- (2) The second harmonic is physically interesting because it is thought to correspond with flow, along with others.

4.2.1 Event Plane Flattening Calibration

In order for the event plane to be a useful in making a v_n measurement, the event plane must be calibrated. For the event plane method, a physical assumption is made that the true distribution of Ψ_n angles will be uniform. In other words, there is no preferred event plane angle in heavy ion collisions; on average there should be an equivalent number of events where the event plane is oriented at 0 radians and at $\frac{\pi}{2}$. If the measured Ψ_n distribution is not flat then it could come from a variety of sources such as variations in the efficiency of detecting charged particles as a function of ϕ . Thus, the event plane calibration seeks to restore the Ψ_n distribution to the physical expectation of uniformity.

The method used in this analysis to achieve this is a "re-centering" and "flattening" calibration. In order to better understand this calibration, it is useful to examine an example uncalibrated Ψ_n distribution. The red curve in Fig. 4.2.1 depicts a significant deviation from uniformity in the Ψ_2 distribution which would distort the v_2 measurement. A combination of effects cause there to be a depletion of Ψ_2 values at 0.0 radians and an enhancement at $\frac{\pi}{2}$ radians. The flattening calibration attempts to offset this lack of uniformity by systematically shifting each event's raw Ψ_2 value by an amount corresponding to the amount the Ψ_2 distribution is nonuniform. The more that the raw Ψ_2 distribution is nonuniform, the more significant that the flattening calibration must

systematically shift each Ψ_2 value in order to restore uniformity. Thus, it is in the analyzer's best interest to provide the flattest possible Ψ_2 distribution before performing the flattening calibration.

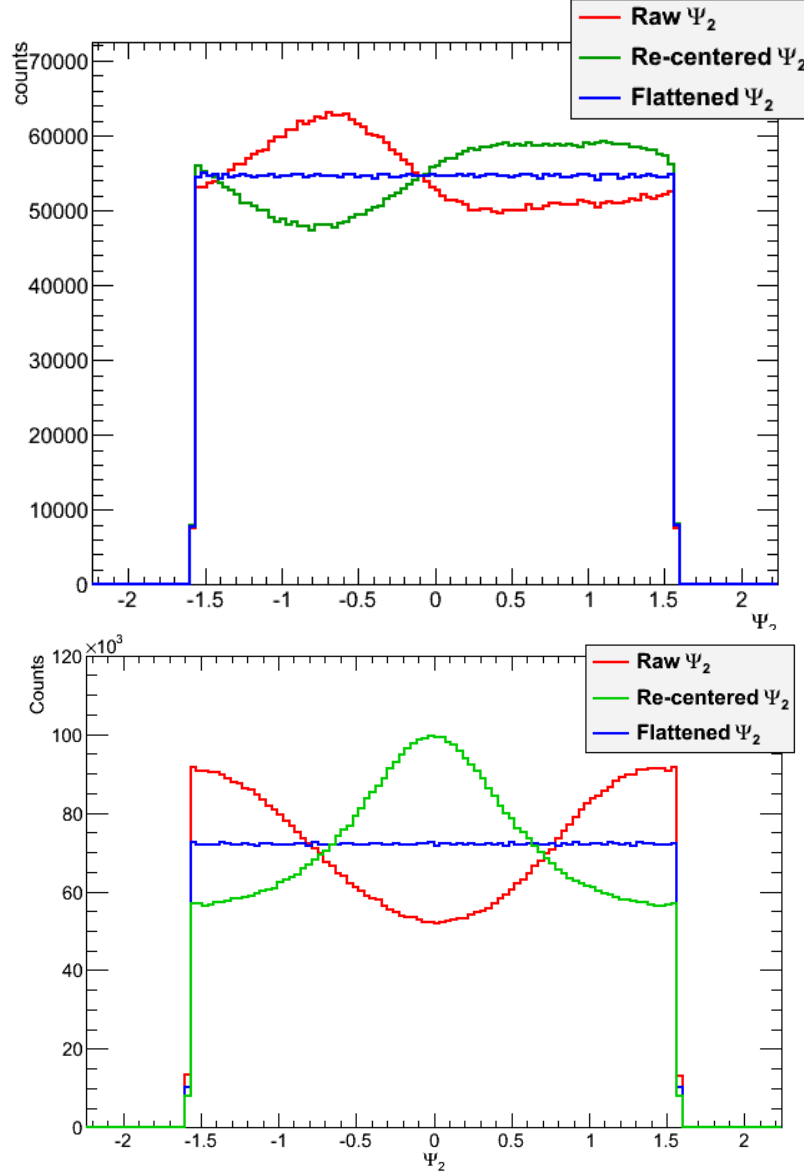


Figure 4.8: This is the Ψ_2 distribution projected over all z-vertex bins at different steps during the calibration. The top is from the FVTX south and the bottom is from the BBC south. The range of the Ψ_2 resolution is from $-\frac{\pi}{2}$ to $\frac{\pi}{2}$ because of the periodicity. The raw (in red) Ψ_2 distribution has a sinusoidal shape. The re-centered (in green) Ψ_2 distribution moves the peak and has a width. The flattened (in blue) Ψ_2 distribution spread out the counts so that there is uniformity. Each calibration step preserves the integral.

The flattening calibration requires two steps to completely flatten the Ψ_n distribution. The first step of the calibration is to re-center the peak of the raw Ψ_n distribution to be at 0.0 radians and to resize the width of the peak. The second step is to Fourier transform the re-centered distribution and use the transformation to shift the Ψ_n values to a uniform distribution. With flattening, each Ψ_n is transformed to $\Psi_n + \Delta\Psi_n$. $\Delta\Psi_n$ is defined as

$$\Delta\Psi_n = \sum_{i=1}^N \left(\frac{2}{i} (\sin(i\Psi) F_i^{\cos}(f(\Psi_n)) - \cos(i\Psi) F_i^{\sin}(f(\Psi_n))) \right), \quad (4.14)$$

where N is the number of components, $F_i^{\cos}(f(x))$ is the i th component of the cosine Fourier transform of $f(x)$, and $f(\Psi_n)$ is the Ψ_n distribution.

For this analysis, $N = 12$ is a sufficient number of components to flatten the Ψ_n distribution. The re-centering and flattening calibration is done in separate 30 z-vertex bins.

4.2.2 Event Plane Resolution Calculation

As mentioned above, the event plane resolution calculation is done using the standard 3-sub event method. The strategy of this method is to leverage the measurement of Ψ_n in different detectors for the same event in order to constrain how well each detector measures Ψ_n . The definition of the event plane resolution is

$$Res(\Psi_n^A) = \sqrt{\frac{\langle \cos(n(\Psi_n^A - \Psi_n^B)) \rangle \langle \cos(n(\Psi_n^A - \Psi_n^C)) \rangle}{\langle \cos(n(\Psi_n^B - \Psi_n^C)) \rangle}}, \quad (4.15)$$

where A,B, and C are three detectors measuring the same event, or each detector measuring a "sub event" assuming no decorrelation [8].

In this analysis, the three detectors that are used are the FVTXs, the BBCs, and the CNT which have η ranges of $-3 < \eta < -1$, $-3.9 < \eta < 3.1$, and $|\eta| < 0.35$ respectively. However, due to the fact that the CNT detector does not have full azimuthal coverage, the CNT event plane is not well defined for a class of events where the event plane doesn't point into the CNT acceptance, therefore the event plane resolution is calculated via a modified yet mathematically equivalent definition to the one mentioned above. This modified method allows the resolution of the FVTX-S

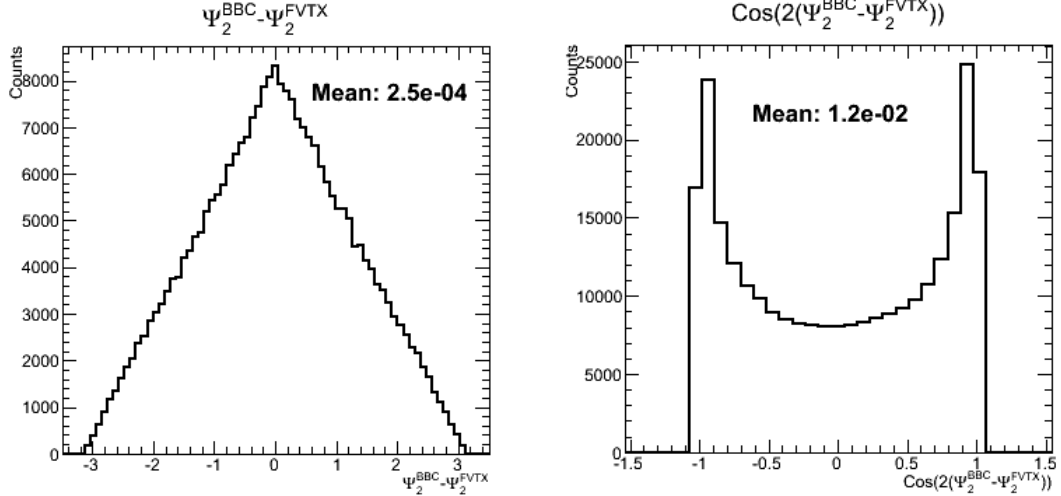


Figure 4.9: The intermediate resolution calculation steps. On the left are the raw difference between the two event planes angles and on the right is the cosine of two times that difference. The average of the distribution on the right is what is used in equation 4.15.

and the BBC-S to be calculated using the CNT without having to calculate CNT event plane. It is defined as

$$Res(\Psi_n^A) = \sqrt{\frac{\langle\langle \cos(n(\Psi_n^A - \phi^{CNT})) \rangle\rangle \langle\langle \cos(n(\Psi_n^A - \Psi_n^C)) \rangle\rangle}{\langle\langle \cos(n(\phi^{CNT} - \Psi_n^C)) \rangle\rangle}}, \quad (4.16)$$

where there is a double average over each CNT track and each event.

Table 4.3:

Detector	$n = 2$	$n = 3$
FVTXs	0.216	0.010
BBCs	0.052	0.010

4.3 Correcting for Beam Geometry

As shown in Fig 4.10, there is an east west difference observed in the measurement of v_2 when using mid-rapidity particles in the west arm ($-1 < \phi < 1$) and in the east arm ($2 < \phi < 4$). The ultimate explanation for this effect comes from beam geometry.

First of all, the collision vertex is significantly offset from the z-axis to which all of the

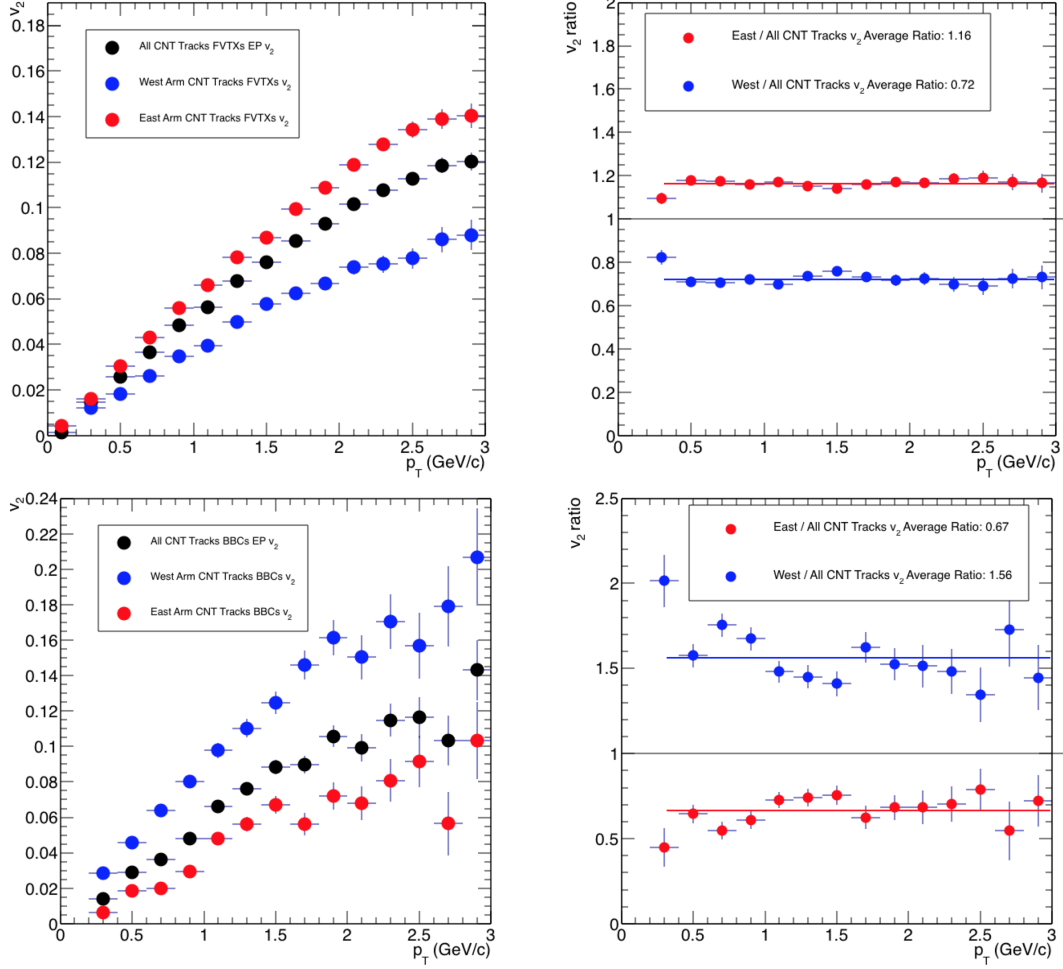


Figure 4.10: The first measurement of v_2 as a function of p_T with the FVTXs (top 2 panels) and the BBCs (bottom 2 panels) event plane for the p+Au @ 200 GeV dataset. The default resolution as shown in table TBA is used. The left panels show the event plane resolution corrected v_2 . The black points show the v_2 measurement measured using all CNT tracks. The blue and red points show the v_2 measurement made with only the west and east arms respectively. It is apparent that there is a significant splitting of the measurement depending on what set of tracks are being used to calculate v_2 which implies there are some systematic errors present. The left panels quantify the level of splitting by plotting the ratio of the east or west v_2 to the measurement made with all CNT tracks. The blue and red lines are constant fits to this ratio and the numbers in the legend are the constant fit parameter. For the FVTXs event plane, the east v_2 measurement is 16% higher on average from the all CNT track measurement and the west measurement is 28% lower on average. For the BBCs event plane, the east v_2 measurement is 56% higher and the west measurement is 33% lower on average.

PHENIX detectors are aligned. The other beam geometry effect, and the more significant of the two effects, comes from the fact that the beams are colliding at an angle of 3.6 milli-Radians in the

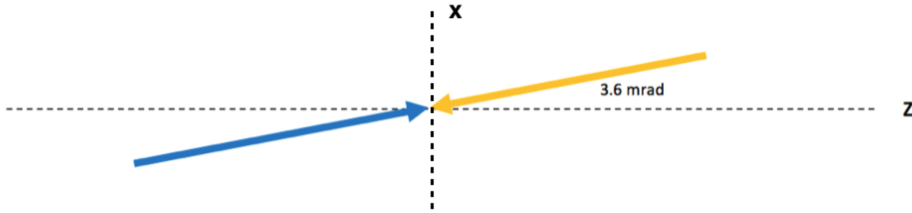


Figure 4.11: A vector diagram illustrating the yellow and blue beam angle colliding at the origin of the x-z plane. The yellow beam stands for the Au-going beam (south-going) and blue beam stands for the p-going beam (north-going). Due to a necessity of running p+Au collisions @ 200 GeV in RHIC, the beams make an angle of 3.6 mRadians with respect to the z-axis in the x-z plane.

x-z plane as shown in Fig 4.11 [2]. The reason a non-ideal beam geometry creates an east west v_2 measurement difference is because of the assumption that the ideal event plane angle is azimuthally isotropic during the event plane flattening calibration. In the translated and rotated frame where the beams are aligned with the z-axis the event plane distribution would be uniform, but in the lab frame the event plane distribution in ϕ would have regions of enhancement and reduction. The event plane flattening calibration algorithm restores a non-uniform distribution to a uniform one; however, if the true event plane distribution is non-uniform then forcing the measured distribution to be uniform would produce systematic errors.

To correct for the collision vertex offset effect the PHENIX detector elements must have their position calculated with respect to the collision vertex rather than the origin and to correct for the beam rotation effect the PHENIX detector elements must be rotated into the beam frame where the beam is aligned with the z-axis. As shown in Fig 4.12, applying these corrections to the event plane when calculating v_2 reduces the magnitude of the splitting but not entirely. The detector elements being in the right place in the beam frame will not completely correct the event plane bias.

To explain this residual effect, consider a cylindrical disk with a hole in the middle centered in the z-axis (which is the shape of the FVTX layers and the BBC) as shown in the left plot of Fig 4.13. For any given ϕ value of the detector, the η range spanned by the disk is the same. However,

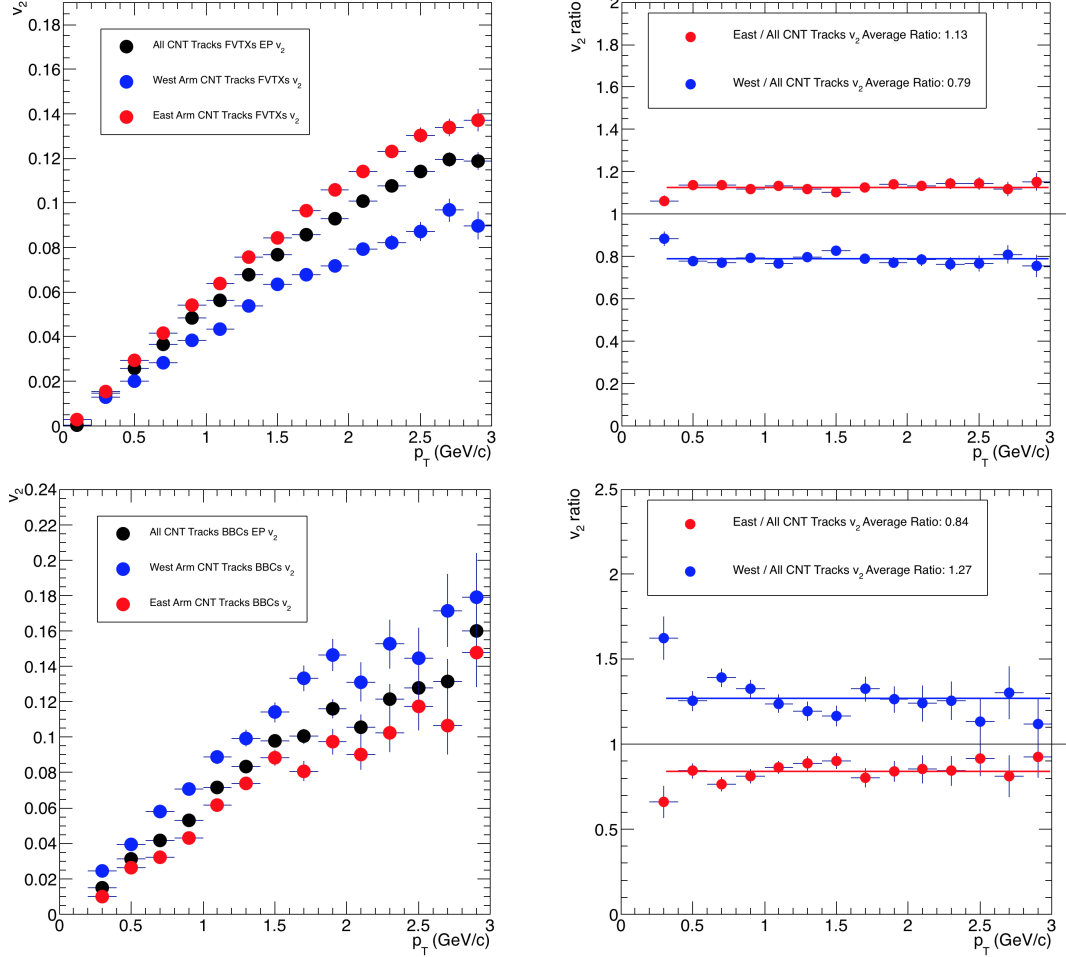


Figure 4.12: A corrected measurement of v_2 as a function of p_T with the FVTXs (top 2 panels) and the BBCs (bottom 2 panels) event plane for the $p+Au @ 200 \text{ GeV}$ dataset. The default resolution as shown in table TBA is used. The plotting conventions are the same as described in the caption of Fig 4.10. Even after correcting for the moving the detector elements back in the right place, it is apparent that there is still a significant splitting of the measurement although there is an improvement. For the FVTXs event plane, the east v_2 measurement is 13% higher on average from the all CNT track measurement and the west measurement is 21% lower on average and for the BBCs event plane, the east v_2 measurement is 27% higher on average and the west measurement is 16% lower on average.

if one were to tilt that disk, the η range spanned by the disk would be ϕ dependent. This tilt would both shift the range in η and increase or decrease the width of the range. Now consider that it is not the disk that is tilted but rather the beam orientation that is tilted. The previous statements about the effect on the η range being ϕ dependent still apply.

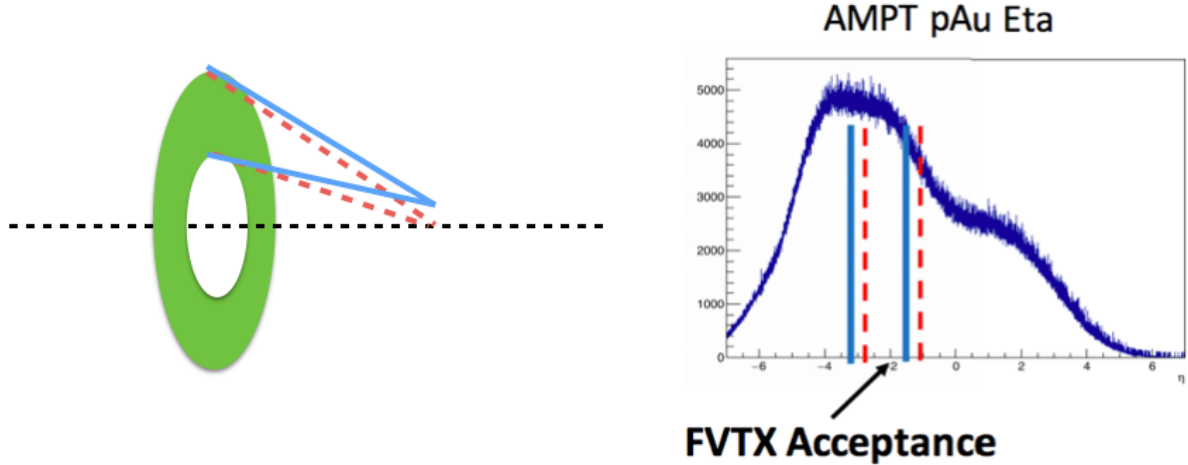


Figure 4.13: On the left is a cartoon diagram illustrating η acceptance shift due to a beam offset in one of the FVTXs layers. The right plot shows the AMPT distribution of particles for pAu @ 200 GeV and the shifted η acceptance.

The combination of the η range changing and the η distribution of charged particles not being flat means that that the average amount of charge particles going through the disk would be systematically ϕ dependent as is illustrated in Fig 4.13. If the average charge particle distribution is not uniform in ϕ , the event plane distribution will not uniform in ϕ which will lead to the flattening procedure creating systematic effects such as the east west v_2 asymmetry. Even if the detector elements are in the right frame, the damage has already been done.

In order to correct for this effect, an additional weight factor is introduced during the event plane calculation. The weight factor is set up in such a way to multiplicatively increase the weighting for hits in ϕ regions with systematically less particles and multiplicatively decrease the weighting for hits in ϕ regions with systematically more particles. The additional weight factor fits in event plane equation in Eqn 4.4 but where w_i is defined as

$$w_i = w_i^D * F(\phi, \text{Vertex}_Z) \quad (4.17)$$

where w_i^D is the default weighting associated with the detector element and $F(\phi, \text{Vertex}_Z)$ is the multiplicative weighting to correct for the beam geometry. $F(\phi, \text{Vertex}_Z)$ is dependent on Vertex_Z in addition to ϕ because η is dependent on the collision vertex. One can analytically calculate this

ϕ dependent weight factor using the geometry of the FVTXs and BBCs as well as using the η distribution of charged particles. Unfortunately, the η distribution of charged particles in pAu @ 200 GeV has not been measured by an experiment so we must rely on models which may be inaccurate.

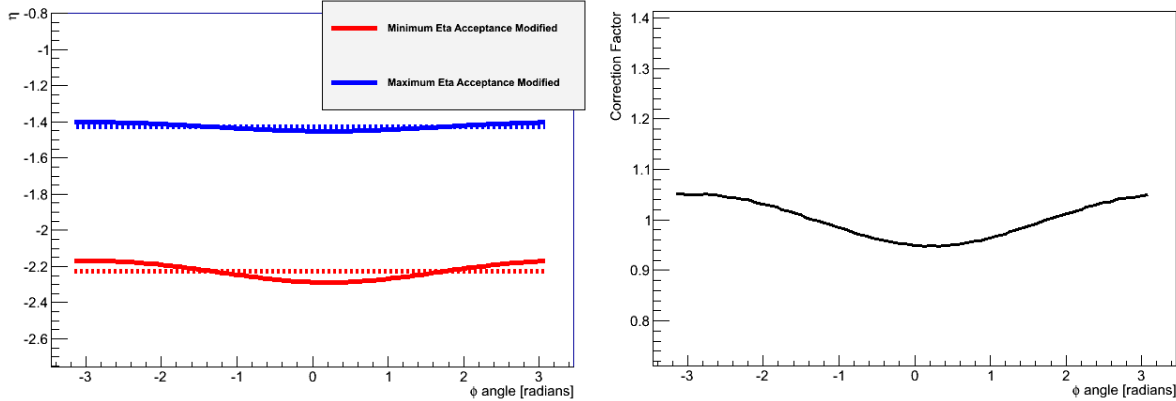


Figure 4.14: The left is the modification of the η acceptance as a function of ϕ for the FVTX first layer. The right is the calculated correction factor from this.

Another way to determine the weight factor is to use a data driven method of measuring to what extent each ϕ region in a detector has systematically more or less particles. Then an inverse weighting based on this measurement is applied to the ϕ regions to correct the detector's ϕ distribution to uniformity. The precise implementation of measuring and applying the uniformity of the ϕ regions in a detector will be examined further in the following sections.

4.3.1 FVTX Inverse Phi Weighting

For this method, the weight factor is determined by plotting all hits in a cylindrical disk detector vs ϕ , normalizing this distribution to one, and then inverting it. When applying this weight factor to the data, it will produce uniform hit distributions in ϕ in the detectors it is applied to. This will, in turn, make the event plane distribution more uniform when measured in those detectors, thus correcting for the effect. The added benefit of using this method is also correcting for hot and cold ϕ regions in the detector. In order to get rid of significant hot or cold ϕ regions, ϕ

regions with weight factors greater than 1.5 or less than 0.5 are set to 0.0. This correction is done for each FVTX layer, in z-vertex bins, and per run. The multiplicative weight function $F(\phi, \text{Vertex}_Z)$ for the FVTX disks is defined as

$$F(\phi, \text{Vertex}_Z, \text{layer}) = \frac{\langle N_{\text{CLUS}}(\text{Vertex}_Z, \text{layer}) \rangle}{N_{\text{CLUS}}(\phi, \text{Vertex}_Z, \text{layer})}, \quad (4.18)$$

where $N_{\text{CLUS}}(\phi, \text{Vertex}_Z, \text{layer})$ is the number of FVTX clusters as a function of ϕ , Vertex_Z , and FVTX layer and $\langle N_{\text{CLUS}}(\text{Vertex}_Z, \text{layer}) \rangle$ is the ϕ average of the number of clusters. The weighting can be seen in Fig 4.15. A comparison between the FVTX weighting and the analytic correction is shown. The good agreement indicates the validity of the weighting.

4.3.2 BBC Charge Weighting

For the BBC, another data driven method is used to correct for the non-uniform particle distribution. Using the distribution of particles in the BBC from the Run15 pp dataset as a baseline, one can apply an inverse weighting much like the one described in the previous paragraph. In the pp dataset, there was no issue with beam colliding at an angle and the average charge across all 64 PMTs in the BBCs is uniform. In this method, the multiplicative weight function $F(\text{PMT}, \text{Vertex}_Z)$ for the BBCs is defined as:

$$F(\text{PMT}, \text{Vertex}_Z) = \frac{\langle N_{\text{Charge}}^{\text{pp}}(\text{Vertex}_Z) \rangle}{\langle N_{\text{Charge}}^{\text{pAu}}(\text{PMT}, \text{Vertex}_Z) \rangle}, \quad (4.19)$$

where $\langle N_{\text{Charge}}^{\text{pp,pAu}}(\text{PMT}, \text{Vertex}_Z) \rangle$ is the event averaged charge as a function of PMT and Vertex_z for the pp and pAu datasets respectively. This weight function is shown in Fig 4.17 and is applied directly to the event plane calculation using Eqns 4.17 and 4.12. Although the weight function could be defined as a function of ϕ like in the FVTX case, the positions of the PMTs in the BBC are fixed and it is more direct to take the ratio between PMTs.

One effect of using this weighting method is that it will make the distribution of particles in the BBC in ϕ and η uniform. This can be illustrated by looking at Fig 4.18. It is apparent that the p+p average charge is much more uniform than the p+Au average charge as a function of ϕ

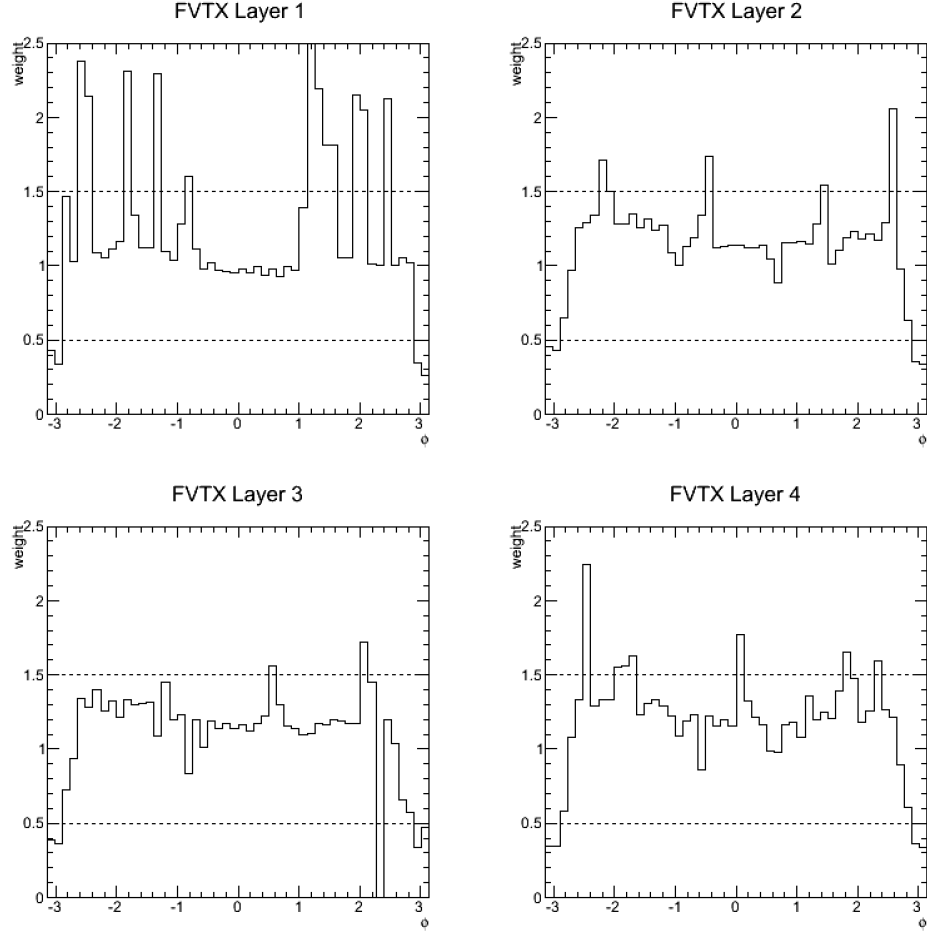


Figure 4.15: These 4 panels show the FVTX ϕ dependent cluster weighting when calculating the FVTX event plane for each layer separately for events with a collision vertex in z is around 0. As you can see there are some ϕ regions where weight factor is outside of the dotted line bounds. This indicates that either there was a severe deficit of clusters measure in the region or excess. Later, we will examine the effect of keeping these regions or cutting them out on the v_2 measurement.

and ring. After applying the p+p/p+Au ratio weighting, which is essentially dividing the left plot by the right plot in Fig 4.18, the PMT charges in ring 1 for the p+Au dataset will be deweighted such that their corrected average charge will be uniform in ϕ and in agreement with the average charge for the other rings. If all the BBC rings have the same average charge, this means that the average charge as a function of η for the BBC will be approximately uniform. This is a reason why for the BBC this method (p+p/p+Au ratio weighting) is preferred, because the variations in the average charge between the rings are normalized. One could apply the FVTX method of inverse

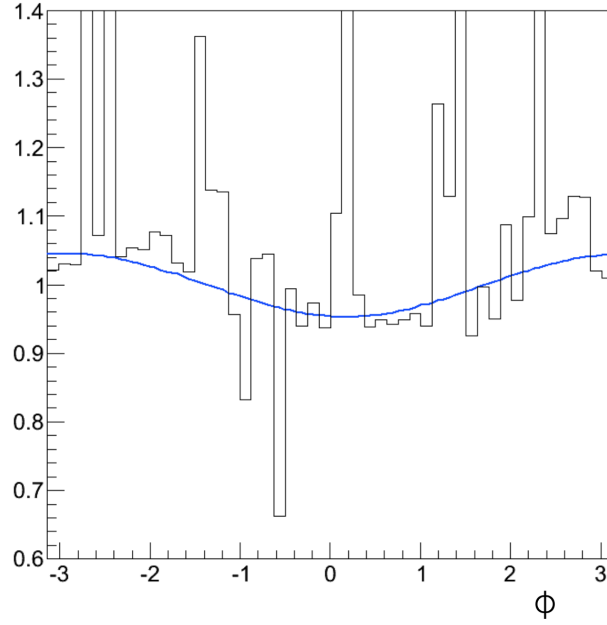


Figure 4.16: The black is the FVTX weighting and the blue is the analytic weighting. They have good agreement.

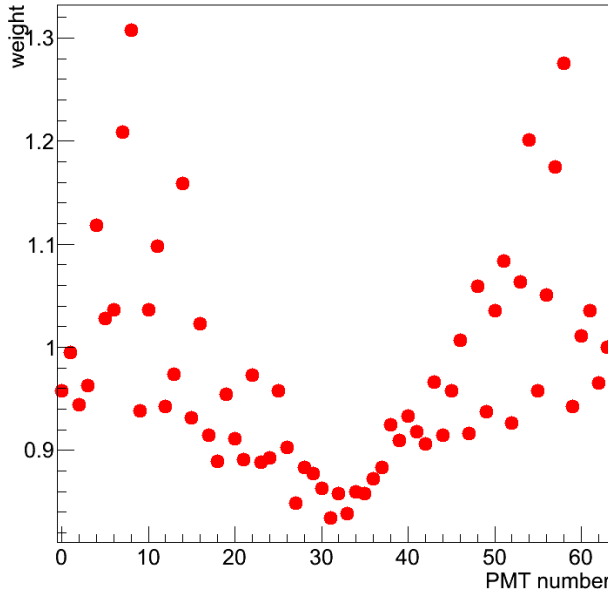


Figure 4.17: Shown here is BBC the multiplicative weight factor F used when calculating the modified event plane for events where the collision vertex in z is around 0. The y-axis is the weight factor and the x-axis is the PMT number for the BBCs (there are 64 total in the BBCs).

ϕ weighting by inverting the right plot of Fig 4.18 to find the weight function. However, although

using only the p+Au dataset would normalize the average charge as a function of ϕ it would not normalize the charge as a function of η . Both methods applied to the data are shown in the next section but the p+p/p+Au ratio method does better.

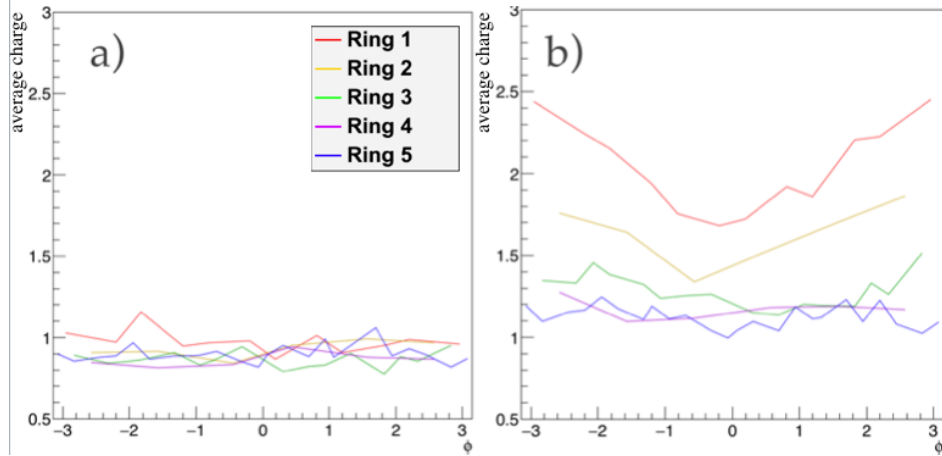


Figure 4.18: These plots depict the average PMT charge per event versus ϕ in the a) the p+p @ 200 GeV and b) p+Au @ 200 GeV. The PMTs are separated by color which corresponds to rings of approximate common radius as shown in Fig 4.7. The left plot shows near uniformity as a function of ϕ and ring. However, the right plot shows a significant deviation from uniformity especially for the innermost rings (rings 1 and 2) there is. In addition to the ϕ variation for the right plot, the innermost rings have the largest average charge when compared to the other rings. This is in part due to the fact the inner most rings cover the a slightly larger η range. However, the innermost rings in the left plot also cover the largest η range and do not exhibit this separation in rings.

4.3.3 Applying Weighting to v_2

When applying the sophisticated weighting to the v_2 measurement, we can quantify how much the weighting corrects the east west v_2 asymmetry. This quantity is calculated by:

$$ratio_{v2} = \frac{\sum_{p_T} east v_2(p_T)}{\sum_{p_T} west v_2(p_T)}, \quad (4.20)$$

and should be closest to 1.0 if the weighting is working. Shown in Fig 4.19 is the correction summary for the FVTX v_2 measurement. The 20% east west deviation is shown in the first column as the black circle. The red, blue and green analytic, inverse ϕ weighting, and inverse ϕ weighting respectively all bring the ratio quantity much closer to 1.0 indicating the weighting techniques are

working. This last statement is true given that we exclude the third layer of the FVTX from our calculation. The rationale for this exclusion is due to FVTX layer three's unusual behavior in relation to the other FVTX layers. As we go from layer 1 to layer 4 the east west ratio quantity generally is trending down except for layer 3. Most likely there is something wrong with the layer data due to electronic or detector problems.

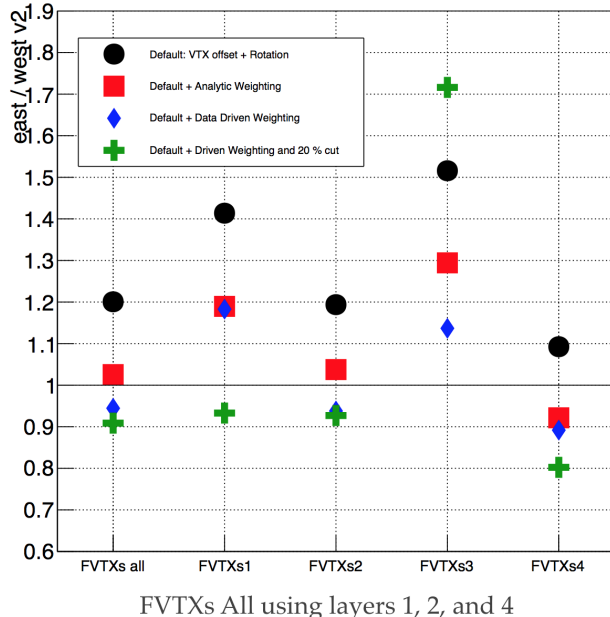


Figure 4.19: Plotted is the FVTX correction summary where the y-axis is the east/west v_2 ratio and the x-axis is the different subset of clusters used to calculate the v_2 . The black markers are with the default corrections as shown in Fig 4.10. The red boxes are the corrections with the analytic weighting shown in Fig 4.14. The blue diamonds are the FVTX inverse ϕ weighting as shown in section 4.3.1. Finally, the green crosses are the same as the blue diamonds except a hot cold filter of 20% was applied additionally. The first column is using all the FVTX layers except for the 3rd layer (which will be explained more later). So the first columns should be approximately the average of columns 2, 3, and 5. Columns 2 through 5 show the ratio calculated from clusters only in that layer. The east west ratio is the worst in layer 3 across all correction methods which is why it was excluded from the first column. The blue, red and green corrections all give equivalent levels of correction.

Fig 4.21 shows the v_2 vs p_T with the green cross correction from Fig 4.19. This figure also shows v_2 vs p_T with the blue diamonds from Fig 4.20. Although the east west ratio does not become exactly 1.0, a ratio value of $\pm 10\%$ of 1.0 is good enough to reduce our systematics errors. This is true for the FVTX points but for the BBC points we never found a weighting scheme to correct

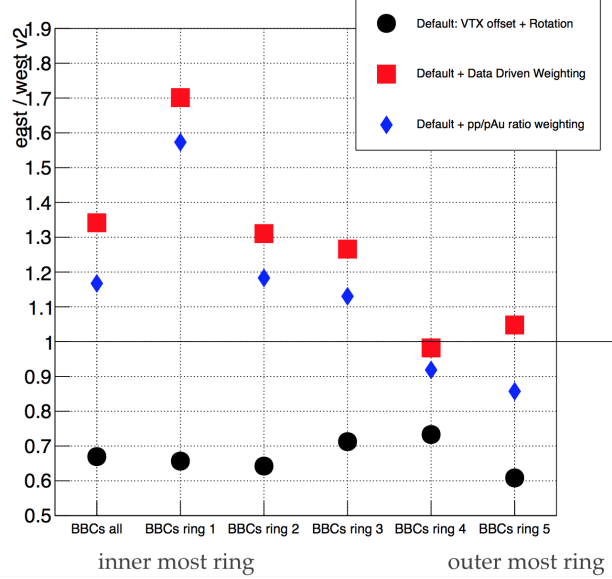


Figure 4.20: Plotted is the BBC correction summary where the y-axis is the east/west v_2 ratio and the x-axis is the different subset of PMTs used to calculate the v_2 . The black markers are with the default corrections as shown in Fig 4.10. The red boxes are the corrections with the analytic weighting shown in Fig 4.14. Finally, the blue diamonds are the BBC inverse ϕ charge weighting as shown in section 4.3.2. The first column is the quantity calculated from all PMTs. columns 2 through 6 are using PMTs from certain rings as defined in Fig 4.7. Ring one is the hardest to correct. The first column should approximately be the average of all the other columns.

the east west ratio to be between 0.9 and 1.1. This is in part why the primary measurement is done using the FVTX.

4.4 Systematic Uncertainties

The main sources of systematic uncertainty in the $v_2(p_T)$ measurement are: (1) track background from photon conversion and weak decays, whose magnitude we determine at 2% relative to the measured v_2 by varying the spatial matching windows in the PC3 from 3σ to 2σ ; (2) Multiple collisions per bunch crossing (i.e., event pile-up) that are observed to occur at an average rate of 8% in the 0%-5% central p+Au collisions. Low luminosity and high-luminosity subsets of the data were analyzed separately and the systematic uncertainty in the $v_2(p_T)$ value is determined to be asymmetric $^{+4\%}_{-0\%}$, since the v_2 values were found to decrease in the events that contain a larger frac-

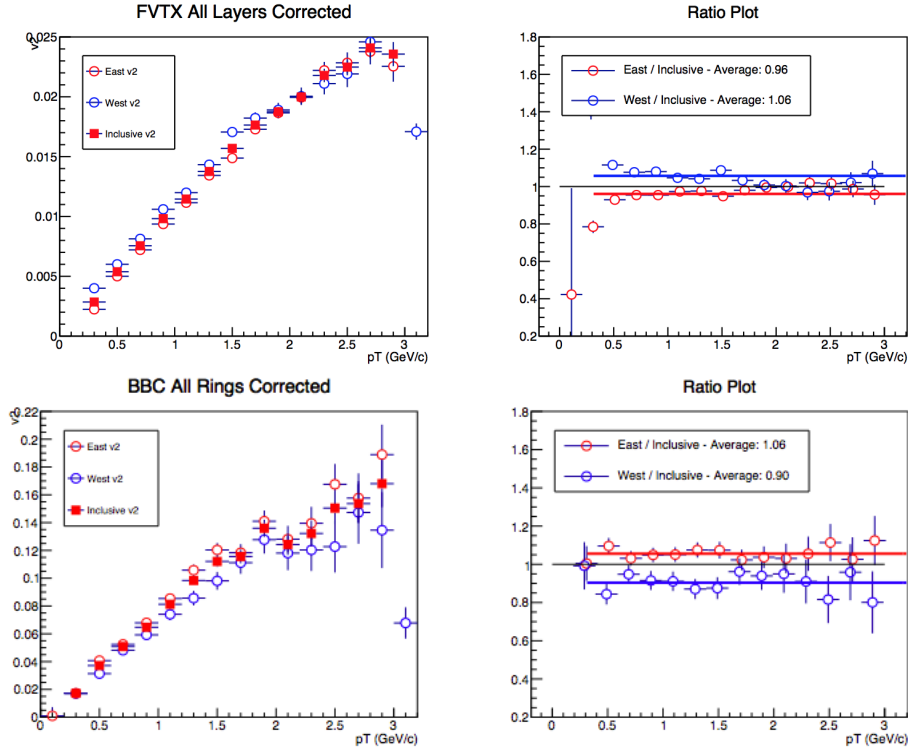


Figure 4.21: The top plots are FVTX event plane measurement corrected with inverse ϕ weighting and 20 % cut. FVTX layer three is excluded. This correction effectively eliminates the east west difference shown on the right.. The bottom plots are BBC event plane measurement corrected with inverse ϕ weighting and 20 % cut. This correction reduces the east west difference significantly.

tion of pile-up, an example of a pile up event is shown in Fig 4.22; (3) Non-flow correlations from elementary processes that enhance the v_2 values, whose contribution we estimate from Fig. 4.23, assigning a p_T -dependent asymmetric uncertainty with a maximum value of $^{+0}_{-23}\%$ for the highest p_T bin. This can be compared to the corresponding $^{+0}_{-9}\%$ [?] and $^{+0}_{-7}\%$ [3] systematic uncertainties in d+Au and $^3\text{He}+\text{Au}$ collisions, respectively; (4) The asymmetry between the east ($\pi/2 < \phi < 3\pi/2$) and west ($-\pi/2 < \phi < \pi/2$) acceptance of the detectors due to an offset of 3.6 mrad between the colliding beams and the longitudinal axis of PHENIX, necessary for running p+Au at the same momentum per nucleon. We applied a corresponding counter-rotation to every central arm track and detector element in the FVTX and BBC, which were also reweighted to restore their uniformity in azimuth. We assign a value of 5% for this systematic uncertainty by taking the difference of

v_2 as measured independently in the east and the west arms after applying the above corrections;

(5) The difference in the $v_2(p_T)$ values when measured independently using the BBC-S and FVTX event planes, which differ by $\pm 3\%$.

Table 4.4 summarizes of all these systematic uncertainties, categorized by type:

- (A) point-to-point uncorrelated between p_T bins,
- (B) point-to-point correlated between p_T bins,
- (C) overall normalization uncertainty in which all points are scaled by the same multiplicative factor.

Table 4.4: Systematic uncertainties given as a percent of the v_2 measurement. Note that the non-flow contribution is p_T dependent and the value here quoted corresponds to the highest measured p_T .

Source	Systematic Uncertainty	Type
Track Background	2.0%	A
Event Pile-up	$+4\%$ -0%	B
Non-Flow	$+0\%$ -23%	B
Beam Angle	5.0%	C
Event-Plane Detectors	3%	C

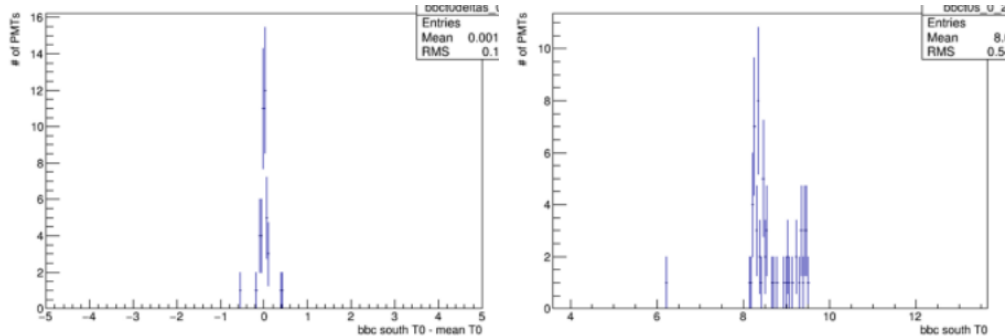


Figure 4.22: The distribution of BBC PMT timing values. The x-axis is the difference between the southern BBC PMT t0 - the mean t0 in the south. The left plot is an example of a normal event, the right plot is an example pile up event. A normal event is strongly peaked at 0. A pile up event has a broad distribution and may not be centered at 0. Pile up events are when 2 or more collisions happen in the same crossing.

4.4.1 Non-Flow

Non-flow is the largest systematic uncertainty. The scaled down reference c_2 is shown as blue squares in Fig. 4.23, panel (a). The ratio of c_2 in the scaled-down p+p reference to that in p+Au is shown in panel (b). From this ratio, as calculated in 4.21, it can be seen that the relative correlation strength in p+Au from elementary processes is at most 23% at the highest p_T . Since this procedure constitutes an approximation to quantify the non-flow correlation strength, it is not subtracted from the total signal, instead it is treated as a source of systematic uncertainty. Even though the p+Au and the p+p baseline data were collected in different years, where potential changes in detector performance could affect our results, it was verified that using p+p data from various run periods has an effect of at most 3% on the calculated non-flow contribution.

$$c_2^{\text{pAu elementary}}(p_T) \simeq c_2^{p+p}(p_T) \frac{(\sum Q^{\text{BBC-S}})_{p+p}}{(\sum Q^{\text{BBC-S}})_{\text{pAu}}} \quad (4.21)$$

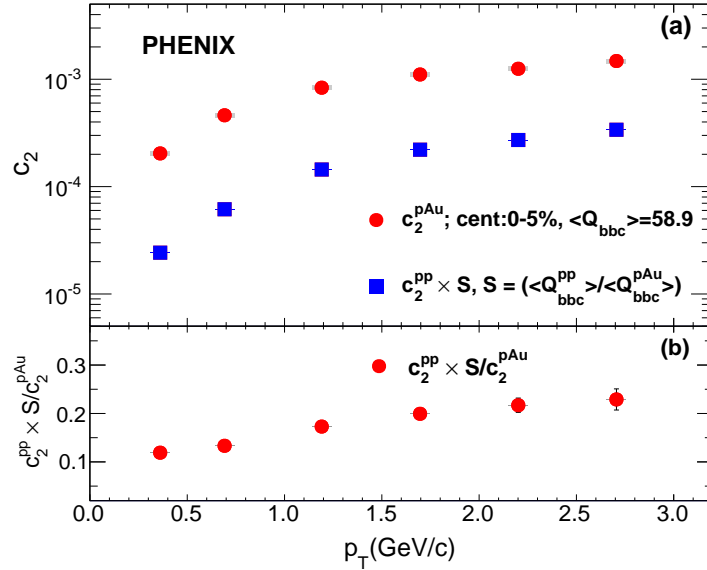


Figure 4.23: (a) The second order harmonic coefficients $c_2(p_T)$ for long range angular correlations in 0%-5% p+Au collisions, as well as for minimum bias p+p collisions. The latter are scaled down by the factor $(\sum Q^{\text{BBC-S}})_{p+p} / (\sum Q^{\text{BBC-S}})_{\text{pAu}}$. (b) The ratio of the two harmonics is plotted with the corresponding statistical errors.

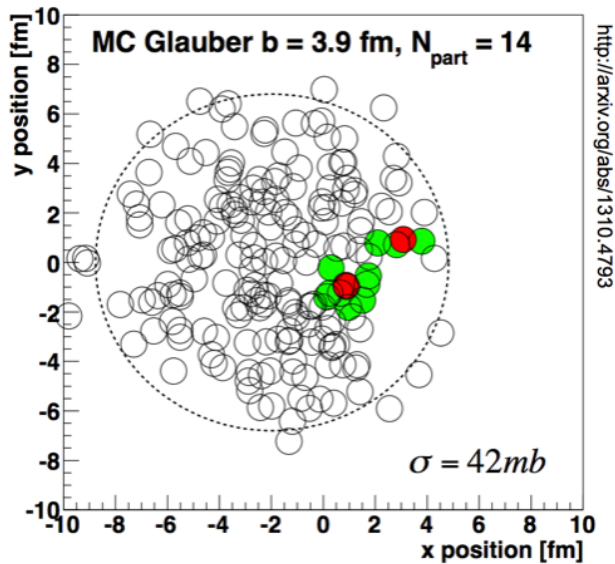


Figure 4.24: TBA

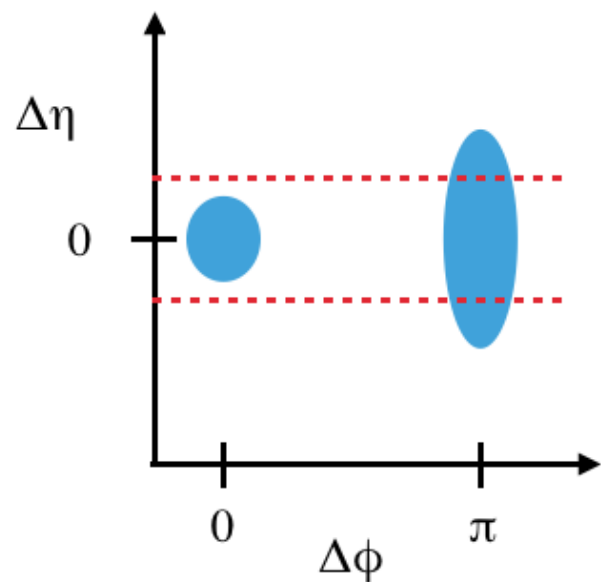


Figure 4.25: TBA

Chapter 5

Results & Discussion

5.1 v_2 Measurement

The resulting v_2 measurement for p+Au @ \sqrt{s} 200 GeV 0–5% centrality shown in 5.1. There is a significant v_2 , even in a small system such as p+Au.

5.2 Comparison with Other Species

We can compare the p+Au v_2 measurement compared to d+Au [add ref] and He+Au [add ref] in the same 0% – 5% centrality class, is shown in Fig. 5.2. The d+Au data, as presented in Ref. [add ref], did not include non-flow contributions in its systematic uncertainties, which are now accounted for in the systematics shown in Fig. 5.2. In all cases, there is a substantial v_2 that rises with p_T . It is notable that the v_2 values for d+Au and He+Au are consistent within uncertainties, as are their eccentricities ε_2 listed in Table 5.1. The p+Au collisions have a significantly lower v_2 and a correspondingly lower calculated ε_2 . At the same time, the ordering of v_2 from p+Au, to d+Au, to He+Au also follows the expected increasing order of particle multiplicity. In the case of d+Au and He+Au, for the 0% – 5% most central events, the published values for midrapidity charged particle density are $dN_{ch}/d\eta = 20.8 \pm 1.5$ and 26.3 ± 1.8 , respectively [add ref]. This quantity has not yet been measured in p+Au collisions.

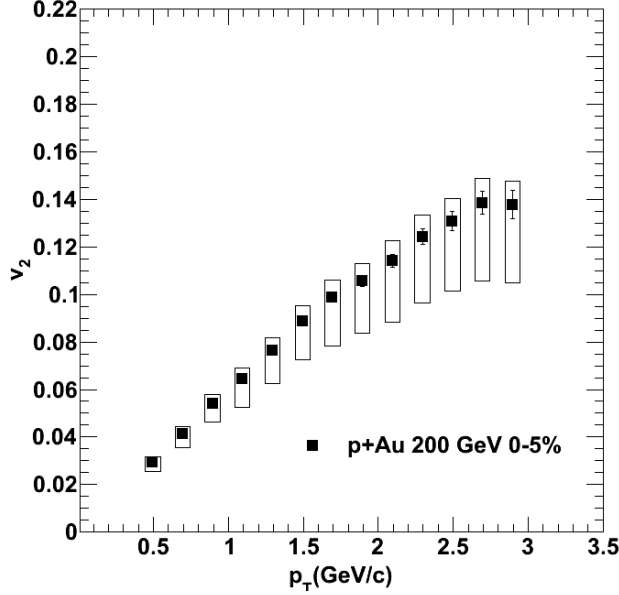


Figure 5.1: The v_2 measurement of $p+Au$ @ $\sqrt{s} = 200$ GeV 0 – 5% centrality. Statistical and systematic errors are shown. The systematic errors are very large especially at high p_t and are dominated by non-flow.

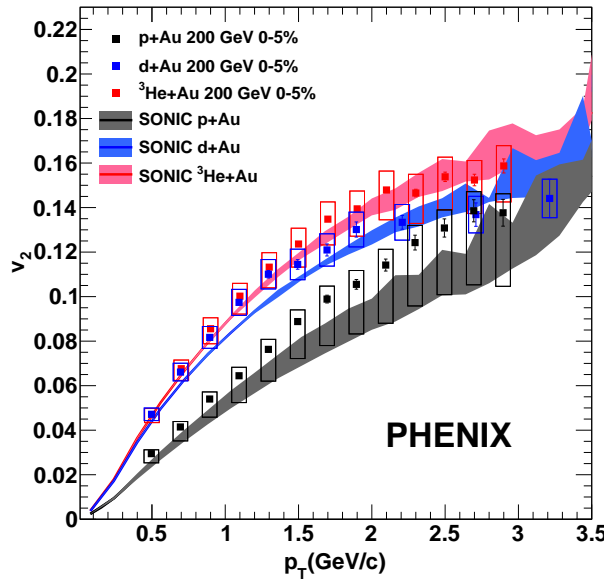


Figure 5.2: v_2 of charged hadrons within $|\eta| < 0.35$ in 0%–5% $p+Au$, $d+Au$, and $HeAu$ central collisions, compared to hydrodynamic calculations using the SONIC model, matched to the same multiplicity as the data. Note that the data points shown include non-flow contributions, whose estimated magnitude is accounted for in the asymmetric systematic uncertainties.

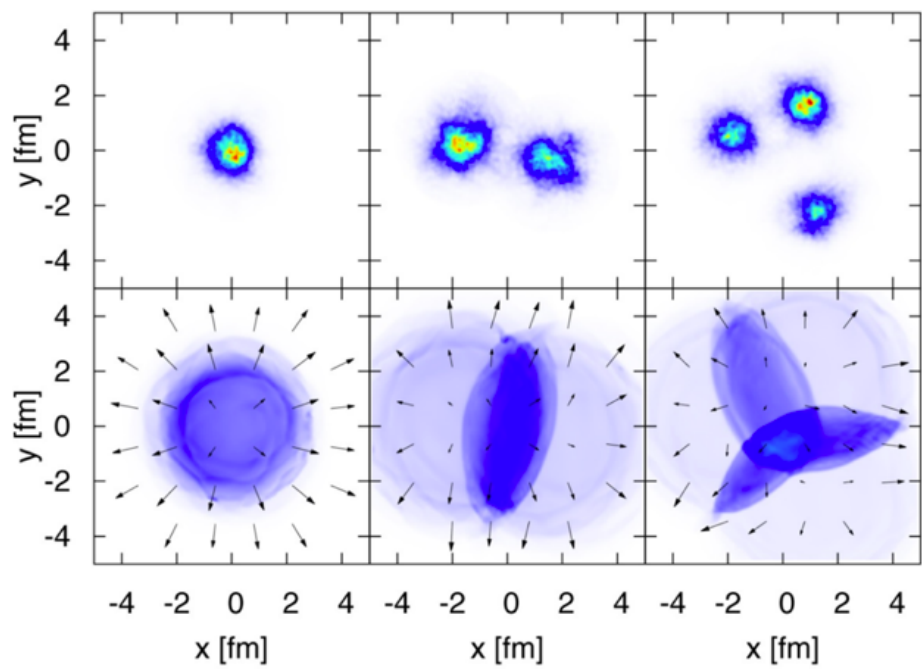


Figure 5.3: TBA

Table 5.1: Initial eccentricity ε_2 of small systems at $\sqrt{s} = 200$ GeV for 0% – 5% centrality from Monte Carlo Glauber initial conditions smeared with a two-dimensional Gaussian of width $\sigma = 0.4$ fm, and IP-Glasma initial conditions.

	p+Au	d+Au	He+Au
Glauber $\langle \varepsilon_2 \rangle$	0.23 ± 0.01	0.54 ± 0.04	0.50 ± 0.02
IP-Glasma $\langle \varepsilon_2 \rangle$	0.10 ± 0.02	0.59 ± 0.01	0.55 ± 0.01

5.3 Comparison with Theory

5.3.1 SONIC

Also shown in Fig. 5.2 are v_2 calculations for each system from the SONIC hydrodynamic model [7], which incorporates standard Monte Carlo Glauber initial conditions followed by viscous hydrodynamics with $\eta/s = 0.08$, and a transition to a hadronic cascade at $T = 170$ MeV. It is notable that these calculations for each system are matched to the charged particle density at midrapidity, with the exact values for 0% – 5% centrality of 10.0, 20.0, and 27.0, for p+Au, d+Au, and He+Au collisions, respectively [7]. Again, note that $dN_{cn}/d\eta$ has not been measured for p+Au, and that the value of 10.0 was extrapolated from measurements in the other two systems [7]. We thus see that the calculation includes both the geometry-related change in eccentricity and the relative collision multiplicity. In all cases, a good agreement is seen within uncertainties between the data and the calculation. These observations strongly support the notion of initial geometry, coupled to the hydrodynamic evolution of the medium as a valid framework to understand small system collectivity.

5.3.2 AMPT

5.3.3 IP-Glasma with Hydro

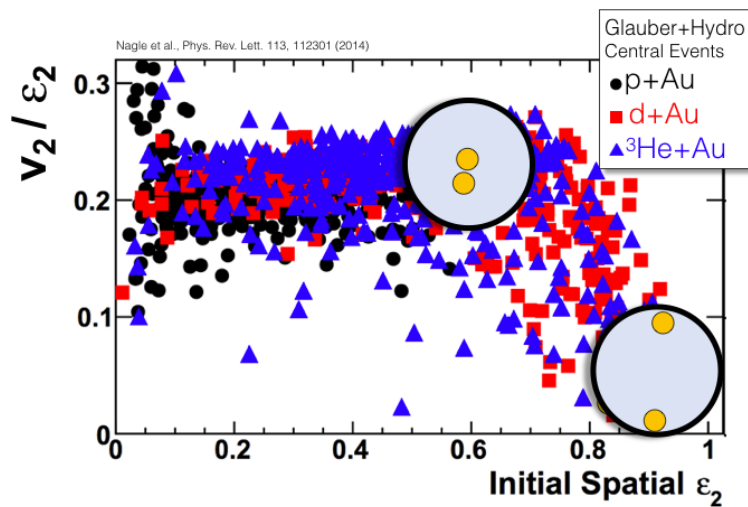


Figure 5.4: TBA

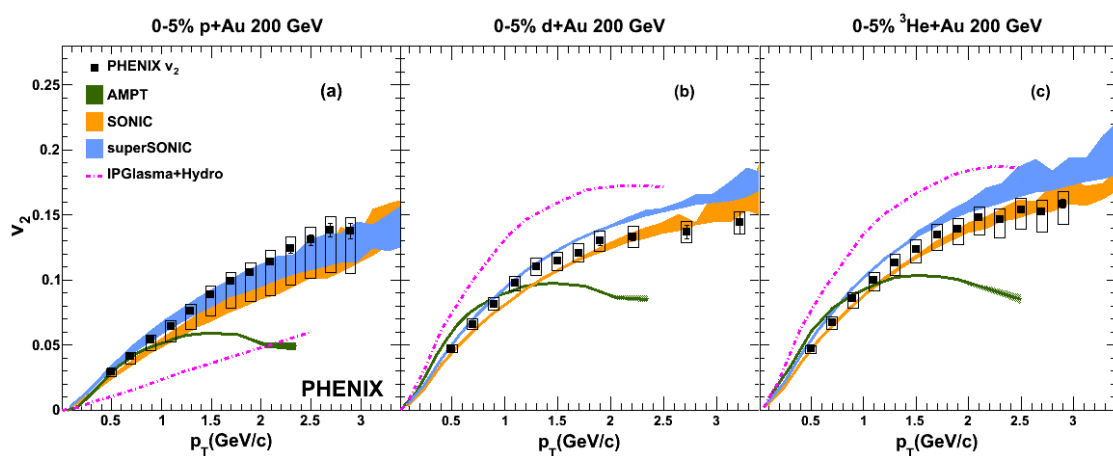


Figure 5.5: TBA

Bibliography

- [1] Event reconstruction in the {PHENIX} central arm spectrometers. Nucl.Instrum.Meth, A482:491–512, 2002.
- [2] Rhic operations with asymmetric collisions in 2015. 2015.
- [3] A. et al Adare. Measurements of elliptic and triangular flow in high-multiplicity ${}^3\text{He} + \text{Au}$ collisions at $\sqrt{s_{NN}} = 200$ GeV. Phys. Rev. Lett., 115:142301, Sep 2015.
- [4] C. Aidala et al. The {PHENIX} forward silicon vertex detector. Nuclear Instruments and Methods in Physics Research Section A: Accelerators, Spectrometers, Detectors and Associated Equipment, 755:44 – 61, 2014.
- [5] K. Adcox et al. {PHENIX} detector overview. Nuclear Instruments and Methods in Physics Research Section A: Accelerators, Spectrometers, Detectors and Associated Equipment, 499(2?3):469 – 479, 2003. The Relativistic Heavy Ion Collider Project: {RHIC} and its Detectors.
- [6] A Fedotov. Progress of high-energy electron cooling for rhic.
- [7] M. Habich, J. L. Nagle, and P. Romatschke. Particle spectra and hbt radii for simulated central nuclear collisions of c+c, al+al, cu+cu, au+au, and pb+pb from $\text{sqrt}(s)=62.4\text{-}2760$ gev. The European Physical Journal C, 75(1):15, 2015.
- [8] A. M. Poskanzer and S. A. Voloshin. Methods for analyzing anisotropic flow in relativistic nuclear collisions. Phys. Rev. C, 58:1671–1678, Sep 1998.
- [9] T. Roser. Rhic performance. Nuclear Physics A, 698(1):23 – 28, 2002.